Intrinsic galaxy alignments from the 2SLAQ and SDSS surveys: luminosity and redshift scalings and implications for weak lensing surveys

Mon. Not. R. Astron. Soc. **381,** 1197–1218 (2007) doi:10.1111/j.1365-2966.2007.12312.x

Intrinsic galaxy alignments from the 2SLAQ and SDSS surveys: luminosity and redshift scalings and implications for weak lensing surveys

Christopher M. Hirata,[1⋆] Rachel Mandelbaum,[1†] Mustapha Ishak,[2] Uroš Seljak,[3,4,5] Robert Nichol,[6] Kevin A. Pimbblet,[7] Nicholas P. Ross[8] and David Wake[8]

[1]*Institute for Advanced Study, Einstein Drive, Princeton, NJ 08540, USA*
[2]*Department of Physics, The University of Texas at Dallas, Richardson, TX 75083, USA*
[3]*Institute for Theoretical Physics, University of Zurich, 8057 Zurich, Switzerland*
[4]*International Centre for Theoretical Physics, Strada Costiera 11, 34014 Trieste, Italy*
[5]*Department of Physics, Princeton University, Princeton, NJ 08544, USA*
[6]*Institute of Cosmology and Gravitation, Mercantile House, University of Portsmouth, Portsmouth PO1 2EG*
[7]*Department of Physics, University of Queensland, Brisbane, QLD 4072, Australia*
[8]*Physics Department, University of Durham, South Road, Durham DH1 3LE*

Accepted 2007 August 1. Received 2007 July 30; in original form 2007 January 27

ABSTRACT

Correlations between intrinsic shear and the density field on large scales, a potentially important contaminant for cosmic shear surveys, have been robustly detected at low redshifts with bright galaxies in Sloan Digital Sky Survey (SDSS) data. Here we present a more detailed characterization of this effect, which can cause anticorrelations between gravitational lensing shear and intrinsic ellipticity (GI correlations). This measurement uses 36 278 luminous red galaxies (LRGs) from the SDSS spectroscopic sample with $0.15 < z < 0.35$, split by redshift and luminosity; 7758 LRGs from the 2dF-SDSS LRG and QSO (2SLAQ) survey at $0.4 < z < 0.8$; and a variety of other SDSS samples from previous, related work. We find $>3\sigma$ detections of the effect on large scales (up to $60\,h^{-1}$ Mpc) for all galaxy subsamples within the SDSS LRG sample; for the 2SLAQ sample, we find a 2σ detection for a bright subsample, and no detection for a fainter subsample. Fitting formulae are provided for the scaling of the GI correlations with luminosity, transverse separation and redshift (for which the 2SLAQ sample, while small, provides crucial constraints due to its longer baseline in redshift). We estimate contamination in the measurement of σ_8 for future cosmic shear surveys on the basis of the fitted dependence of GI correlations on galaxy properties. We find contamination to the power spectrum ranging from -1.5 per cent (optimistic) to -33 per cent (pessimistic) for a toy cosmic shear survey using all galaxies to a depth of $R = 24$ using scales $l \approx 500$, though the central value of predicted contamination is -6.5 per cent. This corresponds to a bias in σ_8 of $\Delta\sigma_8 = -0.004$ (optimistic), -0.02 (central) or -0.10 (pessimistic). We provide a prescription for inclusion of this error in cosmological parameter estimation codes. The principal uncertainty is in the treatment of the $L \leqslant L_\star$ blue galaxies, for which we have no detection of the GI signal, but which could dominate the GI contamination if their GI amplitude is near our upper limits. Characterization of the tidal alignments of these galaxies, especially at redshifts relevant for cosmic shear, should be a high priority for the cosmic shear community.

Key words: gravitational lensing – cosmology: observations – large-scale structure of Universe.

1 INTRODUCTION

Weak gravitational lensing has emerged in recent years as a powerful tool for probing the distribution of matter in the Universe (see e.g. the review by Refregier 2003). Lensing directly traces the matter distribution, and thus is less sensitive to modelling of baryonic

⋆E-mail: chirata@sns.ias.edu
†Hubble Fellow.

physics than other cosmological probes. Because of the relative cleanness of the theory, several groups are engaged in a programme to measure cosmological parameters using the two-point function of weak lensing shear. The field has grown rapidly, with the first detections (Bacon, Refregier & Ellis 2000; Kaiser, Wilson & Luppino 2000; Van Waerbeke et al. 2000; Wittman et al. 2000) giving way to more robust results with smaller statistical errors and better control of observational systematics (Brown et al. 2003; Jarvis et al. 2003; Heymans et al. 2005; Massey et al. 2005). Several of the more recent results provide competitive cosmological constraints (Hoekstra et al. 2006; Jarvis et al. 2006; Sembolini 2006).

In principle, because the cosmic shear signal has the power to constrain the matter power-spectrum amplitude at a particular redshift, it may be a powerful tool to constrain models for dark energy. Splitting source samples into redshift slices, and autocorrelating and cross-correlating each slice against itself and against the other slices can constrain the growth of perturbations as a function of time. Indeed, lensing tomography was shown to put significant constraints on the dark energy parameters (Hu 2002; Huterer 2002; Ishak 2005; Song & Knox 2005) and to have the potential to test gravitational physics on very large scales (Ishak et al. 2006; Knox & Song 2006). Therefore, many future surveys are being planned to have sufficiently high statistical power to measure dark energy using cosmic shear.

The cosmological weak lensing signal is small, with typical shear of the order of 10^{-2} or less, and some of the more ambitious projects under consideration will require measurement of the signal to very high fractional accuracy (<1 per cent). This means that even very small systematic errors can have a significant influence on cosmic shear analyses. One of these systematics is the problem of measuring shape in the presence of an instrumental point spread function (PSF), which can easily introduce spurious ellipticity correlations between different galaxies and dilute existing correlations by making the galaxies appear rounder. There is now a substantial literature on the subject of PSF-induced systematics (Kaiser 2000; Erben et al. 2001; Bernstein & Jarvis 2002; Hirata & Seljak 2003a; Ishak et al. 2004; Vale et al. 2004; Van Waerbeke, Mellier & Hoekstra 2005), including a detailed comparison of different measurement algorithms (Heymans et al. 2006a; Massey et al. 2007). A second problem is the determination of the redshift distribution of source galaxies, d N/d z, which enters into the equation for the cosmic shear power spectrum. There are several ways in which this can be addressed, such as direct spectroscopic measurement of some fields (Bernstein & Jain 2004; Ishak & Hirata 2005; Mandelbaum et al. 2005), self-calibration (Huterer et al. 2006) and possibly in the future by large-scale surveys in the H I 21-cm line (Rawlings et al. 2004). Yet a third potential difficulty is the uncertainty in the theory: the cosmic shear programme places very demanding requirements on the accuracy of N-body simulations, and the effects of baryons will be important on small scales (White 2004; Zhan & Knox 2004; Jing et al. 2006).

Most of the above-described systematics are technical in nature, and in principle can be overcome or at least suppressed with improved modelling and data reduction techniques. Unfortunately, there is another possible systematic in weak lensing, namely intrinsic alignments of the source galaxy population. It has been recognized for some time that if the intrinsic ellipticities of different galaxies are correlated, then this can result in a spurious contribution to the 'shear' power spectrum. Several theoretical models were constructed (Croft & Metzler 2000; Heavens, Refregier & Heymans 2000; Catelan, Kamionkowski & Blandford 2001; Crittenden et al. 2001; Jing 2002) and the intrinsic alignment correlation function was measured by several authors using low-redshift surveys (Brown et al. 2002; Heymans et al. 2004). The severity of this problem is lessened by the fact that such intrinsic ellipticity–intrinsic ellipticity (II) correlations can only exist if the two source galaxies are near each other in physical space, whereas the shape correlations induced by cosmic shear exist between any two galaxies that are near each other in angular coordinates, even if they have a large line-of-sight separation. Thus several authors proposed that galaxy pairs at neighbouring redshifts be downweighted or removed in cosmic shear analyses (King & Schneider 2002; Heymans & Heavens 2003; King & Schneider 2003; Takada & White 2004). However, it was later found that cosmic shear is subject to another type of intrinsic alignment contamination, in which the intrinsic ellipticity of a nearby galaxy correlates with the quadrupole of the density field surrounding it. Since this density field produces a lensing shear on more distant galaxies, it is possible to have a gravitational lensing–intrinsic ellipticity (GI) correlation. The GI correlation can in principle exist between galaxies at very different redshifts, and therefore it cannot be eliminated by considering only shear cross-correlations between different redshift slices (Hirata & Seljak 2004).

The cosmic shear community has proposed several methods for addressing the GI problem, such as marginalization over parametrized models (King 2005; Bridle & King 2007) and removal based on the redshift dependence of the signal (Hirata & Seljak 2004). At the same time, it would be useful to know how large a GI signal to expect, including dependence on the redshift and on the source galaxy luminosity, colour, environment, etc. Models of GI correlation, either empirical or theoretical, would provide an indication of how much of the contaminant needs to be removed in order to realize the full potential of cosmic shear, and would help guide removal strategies (e.g. rejecting certain types of galaxies with the worst GI contamination). At present, there are several analytical (Hui & Zhang 2002; Hirata & Seljak 2004) and simulation-based (Heymans et al. 2006b) models, while observationally the GI correlation function relevant for lensing has been measured only by Mandelbaum et al. (2006a). There is a much larger literature on galaxy alignments that uses statistics other than the GI correlation function, or measures correlations at very small scales (e.g. Pen, Lee & Seljak 2000; Lee & Pen 2001; Bernstein & Norberg 2002; Lee & Pen 2002; Hirata et al. 2004; Navarro, Abadi & Steinmetz 2004; Agustsson & Brainerd 2006; Azzaro et al. 2007; Donoso, O'Mill & Lambas 2006; Yang et al. 2006). These studies are useful for constraining theoretical models, but cannot readily be turned into quantitative empirical estimates of contamination to cosmic shear on large scales.

In a previous paper (Mandelbaum et al. 2006a) we obtained a detection of the large-scale density-ellipticity correlation and presented a preliminary analysis of the expected contamination to cosmic shear results. This paper extends that original work by providing a phenomenological characterization of the intrinsic alignment two-point correlation functions that is as comprehensive as can be obtained with existing data. We use a variety of galaxy samples from the Sloan Digital Sky Survey (SDSS) main spectroscopic sample, the SDSS spectroscopic luminous red galaxy (LRG) sample, and the 2dF-SDSS LRG and QSO (2SLAQ) survey. In particular, we explore the luminosity, colour, environment[1] and redshift

[1] Technically the 'environment dependence of the two-point function' is some combination of higher order statistics, not a two-point function. However, it can be treated by the same methods used to understand colour or luminosity dependence, so we investigate it here.

dependence of the signal. This is an important step in constructing and validating models (either empirical or simulation based) of intrinsic alignments. In this paper we will obtain scaling relations and construct an empirical model for the intrinsic alignment two-point functions for red galaxies; comparison to simulations and consideration of three-point functions will be addressed in a future work.

We begin in Section 2 by reviewing briefly the formalism for describing the cosmic shear and intrinsic alignment correlation functions. The sources of data used for this work are described in Section 3. The methodology used for the measurement is detailed in Section 4. The results obtained and systematics tests are discussed in Section 5. The bias of the LRG samples, needed to estimate the density, is estimated in Section 6. We present power-law fits for the GI correlations in Section 7 and compare against theoretical predictions in Section 8. Using these fitting formulae, we estimate projected contamination for measurements of σ_8 with current and future cosmic shear surveys in Section 9; we discuss how cosmic shear analyses can marginalize over our estimates of GI contamination. We conclude in Section 10. Two appendices are included: Appendix A provides our correlation function data, and Appendix B provides the calculations for converting the Heymans et al. (2006b) simulation results to the variables used in this paper.

2 FORMALISM

The formalism for the analysis of the lensing shear two-point function (Miralda-Escudé 1991) and the intrinsic alignment contamination is well developed. We will briefly summarize the important equations here, and then define some new variables that relate to observables in galaxy surveys. Our notation is consistent with that of Hirata & Seljak (2004) and Mandelbaum et al. (2006a).

2.1 Correlation functions

The observed shear γ of a galaxy is a sum of two components: the gravitational lensing-induced shear γ^G, and the 'intrinsic shear' γ^I, which includes any non-lensing shear, typically due to local tidal fields. Therefore the E mode shear power spectrum between any two redshift bins α and β is the sum of the gravitational lensing power spectrum (GG), the intrinsic–intrinsic and the gravitational–intrinsic terms,

$$C_l^{\rm EE}(\alpha\beta) = C_l^{\rm EE,GG}(\alpha\beta) + C_l^{\rm EE,II}(\alpha\beta) + C_l^{\rm EE,GI}(\alpha\beta). \quad (1)$$

We consider only the E mode since the B mode shear power spectra are much smaller (Cooray & Hu 2002; Schneider, van Waerbeke & Mellier 2002; Cooray, Kamionski & Caldwell 2005). In Mandelbaum et al. (2006a) we presented the Limber integrals that allow us to determine each of these quantities in terms of the matter power spectrum and intrinsic alignment power spectrum. Of greatest interest to us is the GI contamination term,

$$C_l^{\rm EE,GI}(\alpha\beta) = \int_0^{r_{\rm H}} \frac{{\rm d}r}{r^2} f_\alpha(r) W_\beta(r) P_{\delta,\tilde{\gamma}^{\rm I}}\left(k = \frac{l+1/2}{r}\right) + (\alpha \leftrightarrow \beta), \quad (2)$$

where $r_{\rm H}$ is the comoving distance to the horizon, $f_\alpha(r)$ is the comoving distance distribution of the galaxies in sample α, and

$$W_\alpha(r) = \frac{3}{2}\Omega_{\rm m} H_0^2 (1+z) \int_r^{r_{\rm H}} \frac{r(r'-r)}{r'} f_\alpha(r')\,{\rm d}r'. \quad (3)$$

(The generalization of these equations to curved universes can be found in Mandelbaum et al. 2006a.) The power spectrum $P_{\delta,\tilde{\gamma}^{\rm I}}(k)$ is defined as follows. If one chooses any two points in the SDSS survey, their separation in redshift space can then be identified by the transverse separation $r_{\rm p}$ and the radial redshift-space separation Π.[2] The + and × components of the shear are measured with respect to the axis connecting the two galaxies (i.e. positive + shear is radial, whereas negative + shear is tangential). Then one can write the density–intrinsic shear correlation in Fourier space as

$$P_{\delta,\tilde{\gamma}^{\rm I}}(k) = -2\pi \int \xi_{\delta+}(r_{\rm p}, \Pi) J_2(k r_{\rm p})\, r_{\rm p}\, {\rm d}r_{\rm p}\, {\rm d}\Pi, \quad (4)$$

where $\xi_{\delta+}(r_{\rm p}, \Pi)$ is the correlation function between δ and $\tilde{\gamma}^{\rm I}_+$. Here $\tilde{\gamma}^{\rm I}$ is the intrinsic shear weighted by the density of galaxies, i.e. $\tilde{\gamma}^{\rm I} = (1+\delta_{\rm g})\gamma^{\rm I}$, and δ and $\delta_{\rm g}$ refer to the matter and galaxy overdensities, respectively. It is often convenient to do the projection through the radial direction,

$$w_{\delta+}(r_{\rm p}) = \int \xi_{\delta+}(r_{\rm p}, \Pi) {\rm d}\Pi. \quad (5)$$

A similar set of equations can be written for the intrinsic–intrinsic terms; see e.g. equations (5), (7), (9) and (10) of Mandelbaum et al. (2006a).

2.2 Cosmology dependence

Here we note the cosmological model and units adopted for this work and the effect of changing it. Pair separations are measured in comoving h^{-1} Mpc (where $H_0 = 100\,h\,{\rm km\,s^{-1}\,Mpc^{-1}}$), with the angular diameter distance computed in a spatially flat Lambda cold dark matter (ΛCDM) cosmology with $\Omega_{\rm m} = 0.3$. The correlation function measurement depends on $\Omega_{\rm m}$ via the determination of both $r_{\rm p}$ and Π. If $\Omega_{\rm m} \neq 0.3$, then our calculated $r_{\rm p}$ and Π are in error via the equations

$$\frac{r_{\rm p}({\rm calc})}{r_{\rm p}({\rm true})} = \frac{D_{\rm A}(z;\Omega_{\rm m})}{D_{\rm A}(z;0.3)} \quad {\rm and} \quad \frac{\Pi({\rm calc})}{\Pi({\rm true})} = \frac{H(z;0.3)}{H(z;\Omega_{\rm m})}. \quad (6)$$

Note that since angular diameter distance $D_{\rm A}$ is measured in h^{-1} Mpc and Hubble rate $H(z)$ is measured in ${\rm km\,s^{-1}}$ $(h^{-1}\,{\rm Mpc})^{-1}$, there is no dependence of these equations on h. The errors on $r_{\rm p}$ and Π are simple proportionalities and hence when we do power-law fits to the projected correlation function, $w_{\rm g+}(r_{\rm p}) = A r_{\rm p}^{\alpha}$, there is no effect on the power-law index α. The amplitude will however be in error by

$$\frac{A({\rm calc})}{A({\rm true})} = \frac{H(z;0.3)}{H(z;\Omega_{\rm m})} \left[\frac{D_{\rm A}(z;\Omega_{\rm m})}{D_{\rm A}(z;0.3)}\right]^{\alpha}. \quad (7)$$

This equation should be used when interpreting our results in other cosmologies. It should be noted however that the effect is rather small: for $\alpha = -0.8$ (roughly what we observe) and $z = 0.6$ (the cosmology matters most at high redshift), the ratio $A({\rm calc})/A({\rm true}) = 1.05$ for $\Omega_{\rm m} = 0.2$ and 0.96 for $\Omega_{\rm m} = 0.4$. Since this encompasses the range of $\Omega_{\rm m}$ values from recent determinations (e.g. Spergel et al. 2007), the error in our results due to uncertainty in $\Omega_{\rm m}$ is thus at the ∼5 per cent level, which is negligible compared to our final errors. Therefore we have not included it explicitly in our error analysis, and have not attempted to remeasure the correlation function for different cosmologies.

[2] The redshift-space separation is frequently denoted π; we use Π to avoid confusion since the number $\pi = 3.14$ appears frequently in this paper.

3 DATA

Much of the data used here are obtained from the SDSS. The SDSS (York et al. 2000) is an ongoing survey to image $\sim\pi$ sr of the sky, and follow up $\sim 10^6$ of the detected objects spectroscopically (Eisenstein et al. 2001; Richards et al. 2002; Strauss et al. 2002). The imaging is carried out by drift-scanning the sky in photometric conditions (Hogg et al. 2001; Ivezić et al. 2004), in five bands (*ugriz*) (Fukugita et al. 1996; Smith et al. 2002) using a specially designed wide-field camera (Gunn et al. 1998). These imaging data are the source of the large scale structure (LSS) sample that we use in this paper. In addition, objects are targeted for spectroscopy using these data (Blanton et al. 2003a) and are observed with a 640-fibre spectrograph on the same telescope (Gunn et al. 2006). All of these data are processed by completely automated pipelines that detect and measure photometric properties of objects, and astrometrically calibrate the data (Lupton et al. 2001; Pier et al. 2003; Tucker et al. 2006). The SDSS has had six major data releases (Stoughton et al. 2002; Abazajian et al. 2003, 2004; Finkbeiner et al. 2004; Abazajian et al. 2005; Adelman-McCarthy et al. 2006a,b). This analysis uses the spectroscopically observed galaxies in the Value-Added Galaxy Catalogue, LSS sample 14 (Blanton et al. 2005), comprising 3423 deg^2 with SDSS spectroscopic coverage, as well as photometric catalogues to be described below covering a larger area.

To determine density–shear correlation functions, one needs a sample of galaxies that traces the intrinsic shear, and another that traces the density field. Unlike in Mandelbaum et al. (2006a), for this paper we use a variety of galaxy samples spanning redshifts $z = 0.05$–0.8. The sources of these samples are the SDSS main spectroscopic sample ($z = 0.05$–0.2), the SDSS spectroscopic LRG sample ($z = 0.16$–0.36), and the 2SLAQ spectroscopic LRG sample ($z = 0.4$–0.8). In the following subsections we describe each of these samples, and Table 1 summarizes their characteristics. In each of these three redshift regions, the full sample is used to trace the density field, but we break the galaxies down into subsamples based on luminosity and (for the main sample) colour to trace the intrinsic shear field. This enables us to explore the possibility that different types of galaxies show different intrinsic alignment signals.

3.1 SDSS main subsamples

The first samples of galaxies we discuss are those used in Mandelbaum et al. (2006a), subsamples of the SDSS main spectroscopic sample divided by luminosity and other properties. The GI correlation models in this paper are split into early- and late-types, so we have presented here the GI signals for the main galaxies split both by luminosity, and by colour as 'blue' or 'red'. (The differences between the main sample analysis of this section and that of Mandelbaum et al. 2006a are the inclusion of the colour separator, and the use of the full main sample rather than the luminosity subsamples to trace the density field.) For this work, we use the galaxies in L3 through L6, one magnitude fainter than L_* (L3) through two magnitudes brighter (L6). The sample properties were described in full in that paper; for this work, we mention only that the luminosities described are Petrosian magnitudes, extinction corrected using reddening maps from Schlegel, Finkbeiner & Davis (1998) with the extinction-to-reddening ratios given in Stoughton et al. (2002), and k-corrected to $z = 0.1$ using KCORRECT V3_2 software as described by Blanton et al. (2003b).

We use an empirically determined redshift-dependent colour separator of $u - r = 2.1 + 4.2z$, where we use observer frame rather than rest-frame colours; within these luminosity bins, the fraction of red galaxies is 0.40 (L3), 0.52 (L4), 0.64 (L5) and 0.80 (L6).

3.2 SDSS spectroscopic LRGs

Another sample we use is the DR4 spectroscopic LRG sample (Eisenstein et al. 2001). This sample has a fainter flux limit ($r < 19$) than the main sample, and colour cuts to isolate LRGs. We include these galaxies in the redshift range $0.16 < z < 0.35$, for which the sample is approximately volume limited and includes a total of 36 278 galaxies.

In order to study variation within this sample, we use cuts on several parameters. First, we construct luminosities using the r-band model magnitudes, and define three luminosity subsamples as shown in Table 1. The absolute magnitude cuts are defined in terms of $h = H_0/(100\,\mathrm{km\,s^{-1}\,Mpc^{-1}})$ such that one can implement the cuts without specifying the value of H_0. The magnitudes have been corrected for extinction, and are $(k + e)$-corrected to $z = 0$ using the same templates as in Wake et al. (2006). We exclude galaxies lying inside the bright star mask. Random catalogues were generated taking into account the variation of spectroscopic completeness with position. The random points were assigned absolute magnitudes and redshifts drawn from a distribution consistent with the real sample. Shape measurements were obtained via re-Gaussianization for

Table 1. Description of different galaxy samples and their subsamples used for the intrinsic alignment measurements. Included is a sample code and a brief description of the sample, the redshift range spanned, the absolute magnitude and colour cuts [including the redshift to which the absolute magnitude was $(k + e)$-corrected], the magnitude type (P for Petrosian, M for model), and the number of galaxies.

Sample	Sample description	z range	M_r cuts	M_r type	$N_{\rm gal}$
L3	SDSS main L3 (Section 3.1)	$0.02 < z < 0.12$	$-20 \leqslant M_r^{0.1} \leqslant -19$	P	66 312
L4	SDSS main L4 (Section 3.1)	$0.02 < z < 0.19$	$-21 \leqslant M_r^{0.1} \leqslant -20$	P	118 618
L5	SDSS main L5 (Section 3.1)	$0.02 < z < 0.29$	$-22 \leqslant M_r^{0.1} \leqslant -21$	P	73 041
L6	SDSS main L6 (Section 3.1)	$0.03 < z < 0.35$	$-23 \leqslant M_r^{0.1} \leqslant -22$	P	7 937
LRG	SDSS LRG (Section 3.2)	$0.16 < z < 0.35$		M	36 278
LRG1	Cut by magnitude		$M_r^{0.0} \geqslant -22.3$		16 068
LRG2	Cut by magnitude		$-22.6 \leqslant M_r^{0.0} < -22.3$		13 019
LRG3	Cut by magnitude		$M_r^{0.0} < -22.6$		7191
LRG.BG	Cut by environment		BG only		30 849
LRG.non-BG	Cut by environment		Non-BG only		5429
2SLAQ	Full 2SLAQ LRG (Section 3.3)	$0.4 < z < 0.8$		M	7758
2SLAQf	Cut by magnitude		$M_r^{0.0} > -22$	M	3768
2SLAQb	Cut by magnitude		$M_r^{0.0} < -22$	M	3490

96 per cent of this sample (see Section 3.4); the remainder failed due to various problems, such as interpolated or saturated centres.

Besides luminosities, we also use measures of local environment to understand variation of intrinsic alignments within the sample. In particular, one question we may ask is whether intrinsic alignments are properties only of the central galaxy in a halo, or if satellite galaxies have intrinsic alignments as well. Unfortunately it is very difficult to actually measure which galaxies are 'central'. A related quantity that we can measure is whether the galaxy is a brightest group/cluster galaxy (BG) or non-BG. To isolate BGs, we require that a given LRG be the brightest spectroscopic LRG within 2 h^{-1} Mpc projected separation and $\pm$ 1200 km s^{-1}. This cut designates 83 per cent of the sample as BGs and 17 per cent as non-BGs; the 'BGs' are either in the field or host groups and clusters. One limitation to this cut is fibre collisions, for which the relevant radius is 55 arcsec (corresponding to $\sim 200\,h^{-1}$ kpc at the range of redshifts of the sample), which may cause us to mistakenly identify non-BGs as BGs. This is, however, only relevant on small scales. We emphasize that this distinction between BGs and non-BGs does not place any significant constraint on the 'non-BG' galaxy luminosity, which may be quite close to the BG luminosity; the median luminosity gap is 0.3 mag. Unfortunately, the sample of non-BGs is too small to obtain meaningful results when splitting by luminosity gap. It is encouraging that our 'non-BG' fraction of 0.17 agrees with the satellite fraction estimated from halo modelling of the LRG three-point function (Kulkarni et al. 2006). However, in interpreting the results, it must still be remembered that there could be cases where the BG is not actually the central galaxy (in some cases, such as merging clusters, there may not even be such a thing as a 'central' galaxy), and that our selection is restricted to LRGs. In principle one could have increased the signal-to-noise ratio for the non-BGs by increasing the transverse separation cut to $> 2\,h^{-1}$ Mpc so as to obtain equal numbers in the BG and non-BG samples, but this would have had the undesired effect of cutting on large-scale environment (i.e. far beyond the virial radius), thereby including many central galaxies in the 'non-BG' sample.

Finally, in order to constrain redshift evolution more tightly, we have split each of the three LRG luminosity samples at $z = 0.27$ to create a total of six spectroscopic LRG samples.

3.3 2SLAQ LRGs

The 2SLAQ survey has produced samples of roughly 10 000 LRGs with $z_{\rm med} \sim 0.55$ with spectroscopic redshifts, and 10 000 faint quasars. For this paper, we use the 2SLAQ LRGs, which have similar cuts to the SDSS spectroscopic LRG sample, with a fainter apparent magnitude cut of $m_i(\mathrm{model}) < 19.8$ and with a slightly bluer rest-frame colour cut $c_\perp$ than in the SDSS LRG selection.

Cannon et al. (2006) includes further details of the 2SLAQ selection and observation; Wake et al. (2006) shows a first analysis of the LRG luminosity function evolution using this sample in comparison with the SDSS spectroscopic LRG sample. While roughly 10 000 LRG redshifts have been measured, several of our criteria reduce the sample size: we require that they pass the cuts to be in the LRG primary sample (Wake et al. 2006, sample 8) rather than secondary sample (sample 9, which has far lower completeness); we eliminate repeat observations; we reject those in fields with significant incompleteness; we reject those with poor redshift quality; we require that those with redshifts lie in the range $0.4 < z < 0.8$; we require that they have shape measurements with sufficiently high resolution factor (Section 3.4). The last of these cuts reduces the final sample from the canonical 8656 to 7758 galaxies. Random catalogues with the same completeness as a function of angular and radial position as the real sample were used for the random points.

Due to the faintness of this sample, we use model magnitudes. These are $(k + e)$-corrected to $z = 0$ using predictions derived from Bruzual & Charlot (2003); the limitations of these models in describing this sample are discussed more fully in Wake et al. (2006).

3.4 Ellipticity data

In addition to a sample of galaxies, we also need their ellipticities. For this purpose, we use the measurements by Mandelbaum et al. (2005), who obtained shapes for more than 30 million galaxies in the SDSS imaging data down to extinction-corrected magnitude $r = 21.8$ (i.e. far fainter than the spectroscopic limit of the SDSS). A minor modification to the REGLENS pipeline as described in Mandelbaum et al. (2006a) was also used.

The REGLENS pipeline obtains galaxy images in the r and i filters from the SDSS 'atlas images' (Stoughton et al. 2002). The basic principle of shear measurement using these images is to fit a Gaussian profile with elliptical isophotes to the image, and define the components of the ellipticity

$$(e_+, e_\times) = \frac{1-(b/a)^2}{1+(b/a)^2}(\cos 2\phi, \sin 2\phi), \tag{8}$$

where b/a is the axis ratio and ϕ is the position angle of the major axis. The ellipticity is then an estimator for the shear,

$$(\gamma_+, \gamma_\times) = \frac{1}{2\mathcal{R}}\langle(e_+, e_\times)\rangle, \tag{9}$$

where $\mathcal{R} \approx 0.87$ is called the 'shear responsivity' and represents the response of the ellipticity (equation 8) to a small shear (Kaiser, Squires & Broadhurst 1995; Bernstein & Jarvis 2002). In practice, a number of corrections need to be applied to obtain the ellipticity. The most important of these is the correction for the smearing and circularization of the galactic images by the PSF; Mandelbaum et al. (2005) uses the PSF maps obtained from stellar images by the PSP pipeline (Lupton et al. 2001), and corrects for these using the re-Gaussianization technique of Hirata & Seljak (2003a), which includes corrections for non-Gaussianity of both the galaxy profile and the PSF. A smaller correction is for the optical distortions in the telescope: ideally the mapping from the sky to the CCD is shape-preserving (conformal), but in reality this is not the case, resulting in a non-zero 'camera shear'. In the SDSS, this is a small effect (of the order of 0.1 per cent) which can be identified and removed using the astrometric solution (Pier et al. 2003). Finally, a variety of systematics tests are necessary to determine that the shear responsivity $\mathcal{R}$ has in fact been determined correctly. We refer the interested reader to Mandelbaum et al. (2005) for the details of these corrections and tests.

4 METHODOLOGY

The basic methodology in this paper is very similar to that in Mandelbaum et al. (2006a): we correlate a sample of galaxies against some subset of itself, using the subset to trace intrinsic alignments and the full sample to trace the density field. We use the same set of estimators as in Mandelbaum et al. (2006a), generalizing the LS (Landy & Szalay 1993) estimator commonly used for galaxy–galaxy autocorrelations.

The generalization of this estimator to the galaxy–intrinsic correlation is

$$\hat{\xi}_{\rm g+}(r_{\rm p}, \Pi) = \frac{S_+(D-R)}{\mathrm{RR}} = \frac{S_+D - S_+R}{\mathrm{RR}}, \tag{10}$$

where S_+D is the sum over all pairs with separations r_p and Π of the + component of shear:

$$S_+D = \sum_{i \neq j | r_p, \Pi} \frac{e_+(j|i)}{2\mathcal{R}}, \quad (11)$$

where $e_+(j|\,i)$ is the + component of the ellipticity of galaxy j measured relative to the direction to galaxy i, and $\mathcal{R}$ is the shear responsivity. S_+R is defined by a similar equation. We emphasize that positive ξ_{g+} indicates a tendency to point towards overdensities of galaxies (i.e. radial alignment, the opposite of the convention in galaxy–galaxy lensing that positive shear indicates tangential alignment).

We also generalize this large-scale correlation function estimator to cross-correlations. In this case, we use one sample to trace the intrinsic shear, and other to trace the density field. Thus in equation (10), we find pairs of galaxies such that one is in the shear sample and the other in the density sample, so that the S_+ is determined from the former, and the $D - R$ from the latter; the RR in the bottom is determined using one random point corresponding to the shear sample and the other corresponding to the density sample.

This correlation function estimator is then integrated along the line of sight to form the projected intrinsic shear–density correlation function $w_{g+}(r_p)$. We model this function as a power law, $w_{g+} = Ar_p^{\alpha}$, where fits for A and α are done using the full jackknife covariance matrix.

For this paper, we used the same two software pipelines as in Mandelbaum et al. (2006a) to compute the large-scale density–shear correlations. We independently generalized both pipelines to allow different galaxy samples to be used to trace the intrinsic shear and the density field. In summary, the pipeline for which we present results computes the correlation functions over a $120\,h^{-1}$ Mpc (comoving) range along the line of sight ($-60 < \Pi < +60\,h^{-1}$ Mpc) divided into 30 bins, then integrates over Π. The range of transverse separations is from 0.3 to $60\,h^{-1}$ Mpc, in 10 logarithmic bins. Covariance matrices were determined using a jackknife with 50 regions; as demonstrated there, results were relatively robust to the number of bins, with 100 regions giving approximately the same detection significance as 50 regions. For more details about these pipelines, see Mandelbaum et al. (2006a).

5 RESULTS

In this section we describe the results of the galaxy density–shape correlation functions for the SDSS main samples, the SDSS LRGs, and the 2SLAQ LRGs. The measured correlation functions and their uncertainties and correlation matrices are presented in Appendix A.

5.1 SDSS main sample

Here we present results of the measurements of the galaxy density–shape correlations $w_{g+}(r_p)$ using the main sample split not only into luminosity bins, but also into colour samples. There are eight subsamples total, since we have four luminosity bins and two colour bins. We attempt to address the issue of whether blue galaxies show any density–shape alignment when correlated against the full L3–L6 (all colours), and to place constraints if there is no detection. The GI signal $w_{g+}(r_p)$ for each of the eight subsamples is shown in Fig. 1. Fig. 2 shows the confidence contours for fits to a power law, $w_{g+}(r_p) = Ar_p^{-\alpha}$ as discussed in Mandelbaum et al. (2006a).

As shown, for both colour subsamples there is hardly any detection in L3 and L4, consistent with previous works. There is a hint of a signal in L3 for the red sample: when we fit the whole range of scales to an arbitrary power law there is no detection; however, as we will see in Section 7 if we fit to large scales ($r_p > 4.7h^{-1}$ Mpc) where the bias is expected to be roughly linear, and restrict to the power law $\alpha = -0.73$ observed for the LRGs, there is a marginal (2.4σ) detection. For L5, the detection with the red subsample is robust whereas there is no detection with the blue subsample. For L6, the constraints are weak with the blue sample due to its small size, so while the magnitude of the alignments are consistent with the red subsample, they are also marginally consistent with zero. The rest-frame colour distribution of the L6 blue sample, and the distribution of PHOTO pipeline output frac_deV (a measure

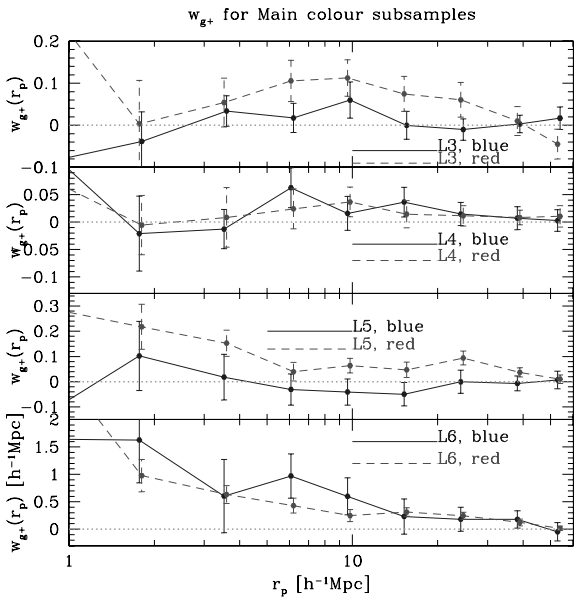

Figure 1. The GI correlation functions for the SDSS main subsamples, split into colour and luminosity bins.

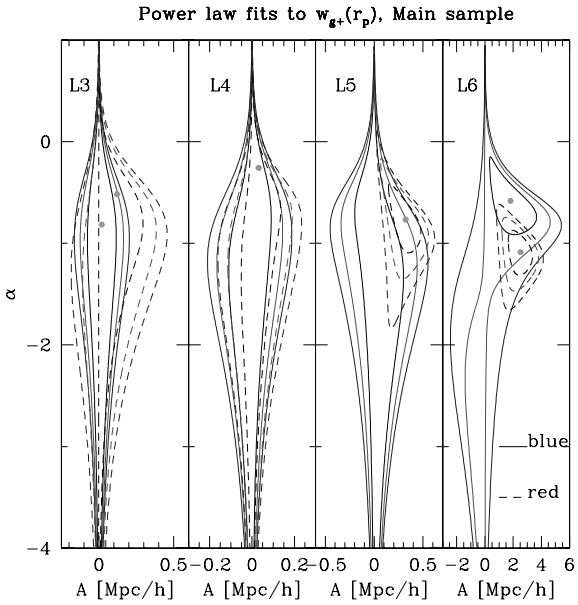

Figure 2. Confidence contours for power-law fits to $w_{g+}(r_p)$ for main sample galaxies. Contours are shown for various subsets of data labelled on the plots; in each case, 1, 2 and 3σ contours are shown.

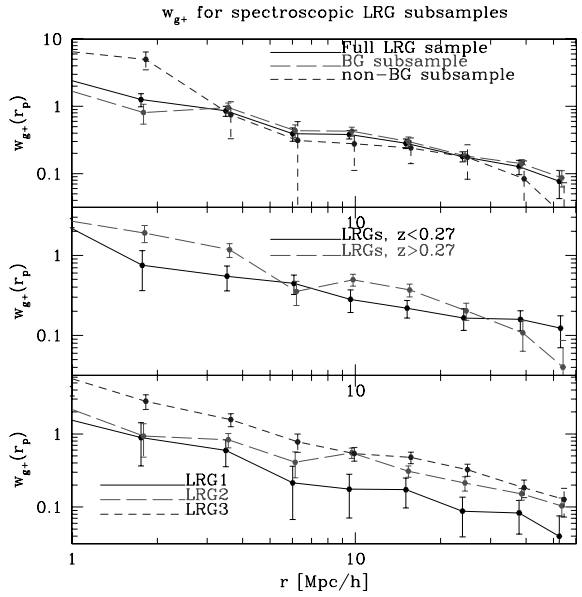

Figure 3. The density–shape correlation function $w_{g+}(r_p)$ from 1 to $60\,h^{-1}$ Mpc with the full spectroscopic LRG sample and various subsamples as labelled on the plot. Errors are 1σ but are somewhat correlated on large scales.

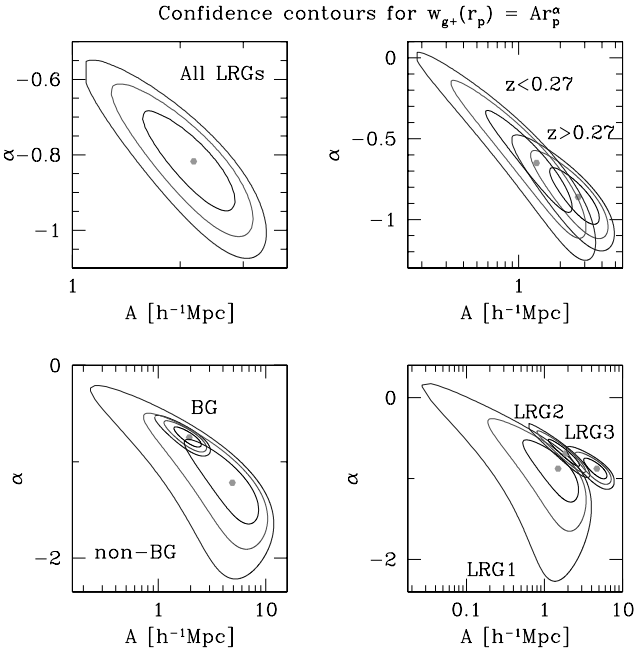

Figure 4. Confidence contours for power-law fits to $w_{g+}(r_p)$ for SDSS spectroscopic LRGs. Contours are shown for various subsets of data labelled on the plots; in each case, 1, 2 and 3σ contours are shown.

of the degree to which a galaxy profile is closer to an exponential or de Vaucouleur profile), suggest that this small L6 blue sample may contain galaxies that are on the edge of the blue versus red galaxy distinction, which could explain this consistency of results.

5.2 SDSS LRGs

Here we present results of the measurements of density–shape correlations for the SDSS spectroscopic LRGs (the measurement is otherwise similar to that of Mandelbaum et al. 2006a). The plots of $w_{g+}(r_p)$ in Fig. 3 are in the same form as in that paper, including 1σ errors. Fig. 4 shows the confidence contours for fits to a power law, $w_{g+} = Ar_p^{\alpha}$.

In the top panel of Fig. 3, we show $w_{g+}(r_p)$ for the full spectroscopic LRG sample, and the BG and non-BG subsamples. As shown, the full sample and the BG subsamples are robustly detected on all scales, out to $60\,h^{-1}$ Mpc. The non-BG subsample has a significantly lower signal-to-noise ratio due to its small size, but the amplitude appears roughly comparable to that of the BG subsamples. In Fig. 4, the contours for the full LRG sample are shown in the upper left-hand panel, and for BGs and non-BGs separately in the lower left-hand panel. As shown there, the constraints on the non-BG sample are indeed quite weak, but the detection is still robust at slightly higher than the 3σ level. The amplitude is higher and the power law steeper than for the BG sample, but is still consistent with it at the 1σ level.

In the middle panel of Fig. 3, we show $w_{g+}(r_p)$ for the spectroscopic LRG sample split at the median redshift. The purpose of this test is that, since this sample is roughly volume limited, with the same luminosity distribution in each of the halves, any evolution in the intrinsic alignment amplitude should be due to redshift evolution. While the amplitude appears higher for the higher redshift sample, the difference is not large; we must see the confidence contours on the fit parameters (which take into account the error correlations) before deciding if the difference is statistically significant, and will also later account for evolution of bias with redshift in Section 7. These contours appear in the upper right-hand panel of Fig. 4, and indicate that the difference is, indeed, not statistically significant.

Finally, the bottom panel of Fig. 3 shows $w_{g+}(r_p)$ for the spectroscopic LRG sample split into luminosity subsamples. These results appear to have roughly the same power-law index, with a multiplicative difference in amplitude, and the confidence contours in the lower right-hand panel of Fig. 4 indicate that this is indeed the case.

5.3 2SLAQ LRGs

In this section, we present results of the measurement of the density–shape correlation using the 2SLAQ LRG sample. Unfortunately, we cannot obtain meaningful results by comparing the full 2SLAQ sample results against the full spectroscopic LRG sample, because the samples do not cover the same range of absolute magnitudes. The 2SLAQ sample is, on average, fainter and bluer than the spectroscopic LRG sample. This difference is problematic since it will tend to give a lower intrinsic alignment amplitude for the 2SLAQ sample that we will need to separate from redshift evolution effects.

To illustrate this point, Fig. 5 shows a comparison of the $(k + e)$-corrected (to $z = 0$) model r-band absolute magnitude distributions of the samples. First, the upper left-hand panel, which shows scatter plots of magnitude $M_r^{0.0}$ versus redshift z. As shown, the spectroscopic LRG sample has roughly constant mean absolute magnitude as a function of redshift for the full redshift range used here. The 2SLAQ sample, on the other hand, shows a trend of being fainter at the low-redshift end and brighter at the high-redshift end. The mean absolute magnitude is roughly 0.2 mag fainter for the 2SLAQ sample than for the SDSS spectroscopic LRG sample (this can also be seen in the bottom right-hand panel, which shows histograms of the absolute magnitude values). This difference is a concern for our work, since in the previous subsection we showed that the intrinsic alignment amplitude has a very strong scaling with luminosity.

One might wonder whether this difference that we observe is due to some systematic, such as uncertainty in the $(k + e)$-corrections.

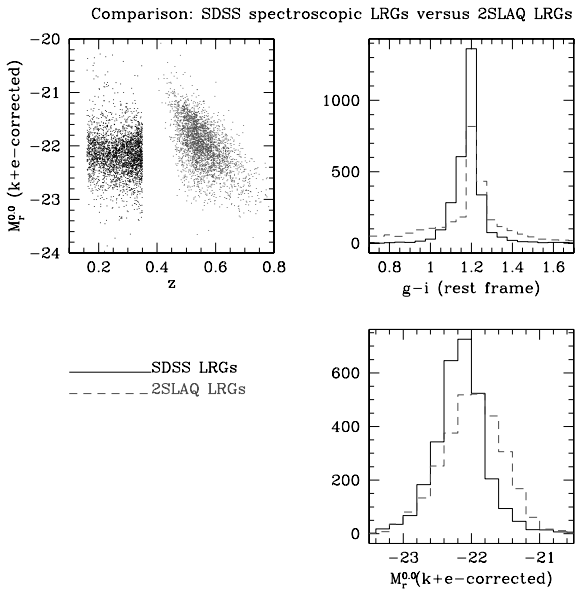

Figure 5. A comparison of the *r*-band absolute magnitudes and colours of the SDSS and 2SLAQ LRG samples. The upper left-hand panel shows the absolute magnitudes as a function of redshift. The upper right-hand panel shows the distribution of $g - i$ rest-frame colour, and the lower right-hand panel shows the absolute magnitude histograms over the full samples.

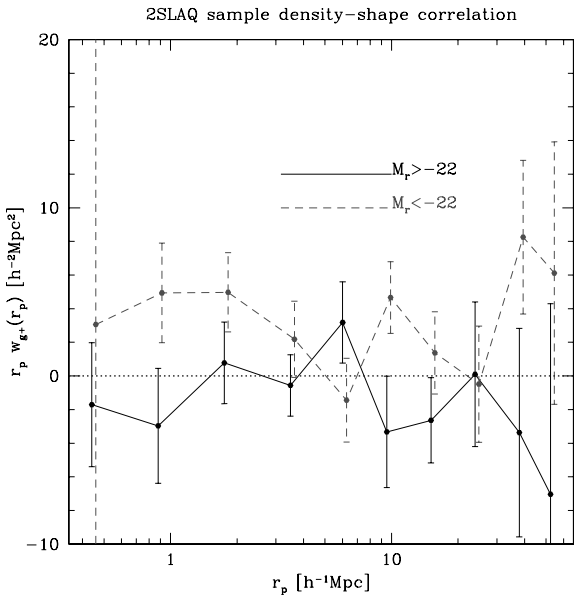

Figure 6. The galaxy density–shape correlation function $r_{\rm p} w_{\rm g+}(r_{\rm p})$ from 1 to 60 h^{-1} Mpc with the luminosity subsamples used to trace the shapes and the full 2SLAQ sample used for the galaxy density *g*. Errors are 1σ but are slightly correlated on large scales.

Wake et al. (2006) explore the difference in more detail, and it does not seem possible to design a plausible model with different formation times, levels of star formation, or other differences that would reduce the difference between the samples to zero. They are inherently different.

Because of this difference between the samples, rather than comparing intrinsic alignment amplitudes directly, we choose instead to fit to a model of the intrinsic alignment amplitude as a function of luminosity and redshift separately. This work can be aided by splitting the 2SLAQ sample into bright and fainter subsets at $M_r = -22$ in addition to using the six redshift and luminosity samples of SDSS spectroscopic LRGs. Fig. 6 shows $r_{\rm p}\ w_{\rm g+}(r_{\rm p})$ for the two 2SLAQ luminosity samples, and Fig. 7 shows the confidence contours for a fits to a power law for each subsample.

Results for the luminosity and redshift-dependent fits will be presented in Section 7.

5.4 Systematics tests

As in Mandelbaum et al. (2006a), we have done several systematics tests to ensure that the detections have not been contaminated by spurious instrumental or other effects. The first is the standard 45° test, whereby we rotate all source ellipticities by 45° before computing the correlation functions (to obtain $w_{\rm g\times}$ instead of $w_{\rm g+}$). This rotated correlation function reverses sign under parity (i.e. the sign of the correlation function is flipped depending on whether one rotates clockwise or counterclockwise) and therefore cannot appear unless there is a systematic, or galaxy formation violates parity invariance.[3] This test was done for the six subsamples of the SDSS spectroscopic LRGs (splitting jointly into three luminosity and two

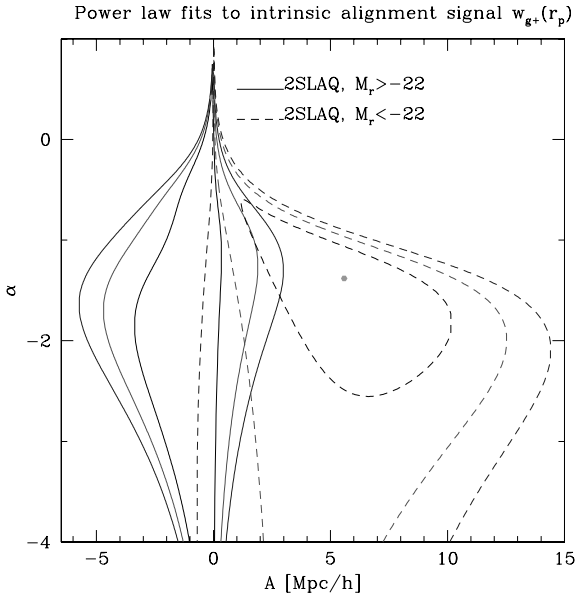

Figure 7. Confidence contours for power-law fits to $w_{\rm g+}(r_{\rm p})$. 1, 2 and 3σ contours are shown for both luminosity subsamples.

redshift bins), for the 'BG' and 'non-BG' subsamples of the SDSS LRGs, and for the two luminosity subsamples of the 2SLAQ LRGs, giving 10 $w_{\rm g\times}$ computations total. For each computed $w_{\rm g\times}$ we computed the χ^2 for a fit to zero signal, and found the associated *p*-values (the probability of getting a larger value of χ^2 by chance). We note that, as in Mandelbaum et al. (2006a), the χ^2 values do not follow the usual χ^2 distribution because of noise in the jackknife covariance matrices. The formalism to describe this effect and account for it with simulations was developed in Hirata et al. (2004). The 10 $p(>\chi^2)$-values computed taking into account the modified

[3] Note that for intrinsic–intrinsic ellpiticity correlations the rotated correlation function $w_{\times\times}$ is parity-allowed and so this would not be a good systematics test; rather one would use $w_{+\times}$, i.e. rotate the ellipticity of only one of the two galaxies in question.

distribution of χ^2 ranged from 0.2–0.94; the lack of very low values indicates that we do not have significant B-mode contamination.

Another test from Mandelbaum et al. (2006a) is the integration of the three-dimensional correlations ξ_{g+} over large line-of-sight separations, $30 < |\Delta\Pi| < 90\,h^{-1}$ Mpc. A signal that is of astrophysical origin should be dominated by the results from smaller $|\Delta\Pi|$, and hence should be consistent with zero for this range. This test will allow us to rule out, e.g. some optical effect causing an apparent alignment of galaxy images (which would not depend on the relative line-of-sight separation). For this test, in all cases, the signal when integrating over large line-of-sight separations was consistent with zero, with $p(>\chi^2)$ values ranging from 0.07 to 0.94.

As in Mandelbaum et al. (2006a), we return to the question of the size of jackknife subsamples. This was primarily a concern for the lower redshift subsamples, for which a jackknife region of a particular size corresponded to a small comoving transverse separation. None the less, despite the higher average redshift of the samples in this paper, we revisit this issue briefly. A particular concern is for the 2SLAQ sample which, while at higher redshift than any of the other samples, also covers a much smaller area overall, so independence of the jackknife regions may be a concern. For the samples used here, changing the number of jackknife samples by a factor of 2 did not change the size of the errors by more than 5–10 per cent, which suggests that we are using the jackknife in a regime where it has converged.

A final concern we may have in comparing results from the SDSS spectroscopic LRG at $z \sim 0.3$ and the 2SLAQ LRGs at $z \sim 0.55$ is that the shape measurements, which are averaged over *r* and *i* bands, are for different sets of rest-frame wavelengths. In principle, these may then be dominated by different stellar populations within the same galaxy that have different intrinsic alignment properties. To test for this effect, we have calculated the analogy of the GI correlation function in equation (10) for SDSS LRGs using the difference between *r*- and *i*-band shears rather than their average as is usually done. Assuming that intrinsic alignments do not vary across this range of wavelengths, this quantity should then be consistent with zero. (We remind the reader that *r* band for the SDSS LRGs corresponds roughly to *i* band for the 2SLAQ LRGs when considering the rest-frame wavelengths.) For the six SDSS LRG subsamples, these correlation functions were consistent with zero, with $p(>\chi^2)$ values ranging from 0.29–0.81.

6 BIAS OF DENSITY TRACERS

To convert the observed w_{g+} to the more relevant (for cosmic shear) $w_{\delta+}$, we need to know the bias of the sample used as the density tracer. This needs to be done for the two LRG samples, and for the SDSS main sample. Due to the much higher signal-to-noise ratio in the LRG samples, we have measured the bias from the LRG projected autocorrelation function. The SDSS main sample has a much lower signal-to-noise ratio detection of GI alignments, and so we have constructed a crude bias estimate by combining previously published results.

6.1 LRGs

Besides computing w_{g+}, our code computes w_{gg}, the galaxy–galaxy autocorrelations. We have compared our results for the full SDSS spectroscopic LRG sample with those in Eisenstein et al. (2005) and Zehavi et al. (2005) and found agreement at the 1σ level. Likewise, our results for the 2SLAQ sample are consistent with those in Ross et al. (2006), though the central value of derived bias does not precisely agree due to significantly different analysis methodologies. We determine consistency by computing the best-fitting power law to w_{gg} and comparing the χ^2 for our best-fitting parameters versus the χ^2 for the best-fitting parameters in Ross et al. (2006), and find $p(>\Delta\chi^2) = 0.2$.

The projected autocorrelations are computed for $0.3 < r_p < 60\,h^{-1}$ Mpc using

$$w_{gg}(r_p) = \int \xi_{gg}(r_p, \Pi)\,d\Pi, \tag{12}$$

where ξ_{gg} has been estimated using the LS estimator,

$$\hat{\xi}_{gg}(r_p, \Pi) = \frac{(D-R)^2}{RR} = \frac{DD - 2DR + RR}{RR}. \tag{13}$$

Integration along the Π direction is carried out for $-60 < \Pi < +60\,h^{-1}$ Mpc. As for the w_{g+} calculations, covariance matrices are determined using a jackknife with 50 regions.

We did three types of fits to obtain the bias from w_{gg} for each of the four samples (low-*z* SDSS LRGs, high-*z* SDSS LRGs, faint 2SLAQ LRGs and bright 2SLAQ LRGs). The first method is to fit the bias *b* to the linear correlation function,

$$w_{gg}(r_p) = b^2 \int \frac{k\,dk}{2\pi} P_{lin}(k) W_{r_p}(k) + C. \tag{14}$$

The second method is to use the Q model from Cole et al. (2005),

$$w_{gg}(r_p) = b^2 \int \frac{k\,dk}{2\pi} P_{lin}(k) \frac{1+Qk^2}{1+Ak} W_{r_p}(k) + C, \tag{15}$$

where for a real-space power spectrum $A = 1.7\,h^{-1}$ Mpc (Cole et al. 2005); the χ^2 is minimized with respect to both *b* and *Q*. The third method is to use equation (14) but with the non-linear power spectrum instead of the linear. The window function for two-dimensional projection for an infinitesimally thin range in radius is simply a Bessel function: $W_{r_p}(k) = J_0(kr_p)$. For a finite range in r_p, the window function is the weighted average (by area) over r_p:

$$\begin{aligned} W_{r_p}(k) &= \frac{\int_{r_{p,\min}}^{r_{p,\max}} 2\pi r_p J_0(kr_p)\,dr_p}{\int_{r_{p,\min}}^{r_{p,\max}} 2\pi r_p\,dr_p} \\ &= \frac{2[J_1(kr_{p,\max}) - J_1(kr_{p,\min})]}{k^2(r_{p,\max}^2 - r_{p,\min}^2)}. \end{aligned} \tag{16}$$

The constant *C* accounts for the effect of the integral constraint on the numerator of equation (13). There are in principle additional corrections associated with the uncertainty in the denominator (see Hui & Gaztañaga 1999, for a thorough discussion), which are relevant if the correlation function is of the order of unity on the scale of the survey region. This is not the case here so we have not included them.

We used the '*Wilkinson Microwave Anisotropy Probe* (*WMAP*) + all' ΛCDM cosmology (Spergel et al. 2007) for the bias determinations, which has $\Omega_m = 0.262$, $h = 0.708$, $\Omega_b = 0.0437$, $n_s = 0.938$ and $\sigma_8 = 0.751$; in general for other values of σ_8, the bias scales as $b \propto \sigma_8^{-1}$. The projected correlation functions and best-fitting Q models are shown in Fig. 8. The linear theory fit used the Eisenstein & Hu (1998) transfer function; the two non-linear fits differ only in their use of the non-linear mappings of either Peacock & Dodds (1996) or Smith et al. (2003).

The biases of the LSS tracers are displayed in Table 2; note that two values of the minimum r_p were used, with the linear fit restricted to the largest scales. The b_g values are consistent with each other and the χ^2 values are reasonable. The *Q* values obtained with the

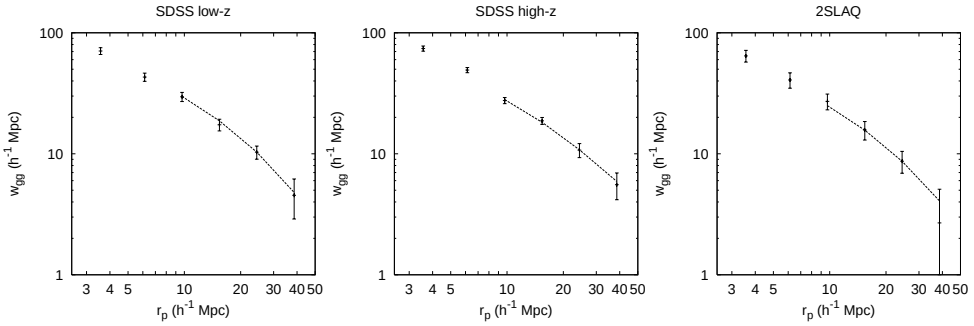

Figure 8. The projected galaxy–galaxy correlation functions $w_{\rm gg}(r_{\rm p})$ for the three samples and the best-fitting non-linear power spectrum (using the Smith et al. 2003 mapping) to the 7.5–47 h^{-1} Mpc. Note that the error bars are correlated.

Table 2. The bias of the various tracer samples for four fits. The error estimates are 1σ. The fitting methods are 'lin' (linear theory), 'Q' (Q model), 'PD' (Peacock & Dodds 1996) and 'S' (Smith et al. 2003).

Sample	$r_{\rm p}$ range (h^{-1} Mpc)	Method	$b_{\rm g}$	χ^2/d.o.f.
SDSS low-z	12–47	lin	1.84 ± 0.15	0.924/1
$\langle z \rangle = 0.22$	7.5–47	Q	2.05 ± 0.12	0.809/1
	7.5–47	PD	1.97 ± 0.12	1.476/2
	7.5–47	S	2.01 ± 0.12	1.428/2
SDSS high-z	12–47	lin	1.94 ± 0.09	0.001/1
$\langle z \rangle = 0.31$	7.5–47	Q	1.97 ± 0.08	0.068/1
	7.5–47	PD	1.93 ± 0.07	1.405/2
	7.5–47	S	1.97 ± 0.07	1.257/2
2SLAQ	12–47	lin	1.98 ± 0.25	0.879/1
$\langle z \rangle = 0.55$	7.5–47	Q	2.22 ± 0.24	0.798/1
	7.5–47	PD	2.10 ± 0.20	1.026/2
	7.5–47	S	2.13 ± 0.20	0.953/2

Table 3. The effective bias $b_{\rm eff}$ of the L3–L6 density tracer used in the GI correlation analysis. As explained in the text, $b_{\rm eff}$ depends on the SDSS main subsample used to trace the ellipticity field because the sample is not volume limited. Values are normalized to *WMAP* ($\sigma_8 = 0.751$); for other values of σ_8, these values should be rescaled as $b_{\rm eff} \propto \sigma_8^{-1}$. The weighted effective redshift $z_{\rm eff}$ at which the correlation is measured is defined by replacing b_δ in equation (17) with z.

Ellipticity tracer	$b_{\rm eff}$	$z_{\rm eff}$
L3.red	1.08	0.07
L3.blue	1.08	0.07
L4.red	1.11	0.09
L4.blue	1.12	0.09
L5.red	1.14	0.10
L5.blue	1.16	0.12
L6.red	1.16	0.12
L6.blue	1.19	0.13

Q-model fits are 61 ± 48 (SDSS low-z), -24 ± 49 (SDSS high-z) and 50 ± 128 (2SLAQ), i.e. Q is poorly constrained at these scales but is consistent with other determinations for similar galaxy types (Padmanabhan et al. 2006).

As a systematics test, we also computed the integral $\int \xi(r_{\rm p}, \Pi)\,{\rm d}\Pi$ over the range $60 < |\Pi| < 120\,h^{-1}$ Mpc and computed $b_{\rm g}^2$ using this in place of $w_{\rm p}(r_{\rm p})$. (For the fit we used the Smith et al. 2003 non-linear mapping.) In the absence of systematics, this should give a result close to zero since the galaxies considered are well separated along the line of sight, but could be non-zero if (for example) there are spurious angular fluctuations in the galaxy distribution. The procedure gives '$b_{\rm g}^2$' values of $+0.07 \pm 0.15$, -0.06 ± 0.16, and $+0.17 \pm 0.34$ (1σ) for the SDSS low-z, SDSS high-z and 2SLAQ samples, respectively. These are all consistent with zero and much less than the actual $b_{\rm g}^2$ values.

For the rest of the paper we have used the biases from the 7.5– $47h^{-1}$ Mpc fit with the Smith et al. (2003) non-linear power spectrum.

6.2 SDSS main sample

The density tracer for the SDSS main sample is the combined L3–L6 sample. The bias of this tracer varies as a function of redshift because the nearby part of the sample is dominated by galaxies with $L \leqslant L_\star$ and the more distant part is dominated by galaxies with $L > L_\star$, which show stronger clustering. This should be taken into account when converting $w_{\rm g+}(r_{\rm p})$ to $w_{\delta+}(r_{\rm p})$; in particular it results in an effective bias $b_{\rm eff}$ that varies according to sample whose intrinsic alignments are being measured: the L3 GI correlation function measurement is dominated by nearby pairs of galaxies, hence $b_{\rm eff}$ is low, while for L6 $b_{\rm eff}$ is high. A very crude way of estimating this effective bias is to take the pair-weighted average of the bias of the density tracer,

$$b_{\rm eff} = \frac{\int b_\delta n_\gamma^{\rm com} n_\delta^{\rm com} {\rm d}V}{\int n_\gamma^{\rm com} n_\delta^{\rm com}\,{\rm d}V}, \qquad (17)$$

where b_δ is the bias of the density tracer, and $n_\gamma^{\rm com}$ and $n_\delta^{\rm com}$ are the comoving number densities of the ellipticity and density tracers, respectively. For the bias of the density tracers, we use the results from Tegmark et al. (2004) and Seljak et al. (2005), namely that $\sigma_8 b = 0.764$ (L3), 0.848 (L4), 0.968 (L5) and 1.427 (L6). The resulting values of $b_{\rm eff}$ for each of the ellipticity tracers are shown in Table 3. The biases of the L3–L6 samples are generally determined to an uncertainty of several per cent; we do not explicitly propagate these uncertainties as they will contribute negligibly to the final error in $w_{\delta+}(r_{\rm p})$.

7 POWER-LAW FITS FOR LRGS

In this section we present an empirical parametrized model for the large-scale GI correlation of LRGs, with power-law dependence on the galaxy's luminosity, redshift (technically $1 + z$), and transverse

separation. It should be noted that such a model is purely empirical, in the sense that it reproduces the correct correlation between the GI amplitude and the specified galaxy properties. This is all that is needed to predict GI contamination for cosmic shear surveys; however, when considering theoretical interpretation of the results presented here, it must be remembered that our fits represent correlations, not causal relationships. For example, we find that the GI amplitude scales as roughly $L^{1.5}$, but this does not mean that the alignment is 'caused by' the galaxy's r-band luminosity – in practice both the GI amplitude and the galaxy luminosity are both products of the process of galaxy formation and hence are correlated. In particular, different scalings might be obtained if we also fit dependence on, e.g. colour, velocity dispersion, surface brightness, etc., since these are correlated with luminosity and redshift.

The simplest model including luminosity, redshift and scale dependence is

$$w_{\delta+}(r_\mathrm{p}) = A_0 \left(\frac{r_\mathrm{p}}{r_\mathrm{pivot}}\right)^{\alpha} \left(\frac{L}{L_0}\right)^{\beta} \left(\frac{1+z}{1+z_\mathrm{pivot}}\right)^{\gamma}. \quad (18)$$

Here there are four parameters $\{A_0, \alpha, \beta, \gamma\}$, and L is the galaxy luminosity. We use the r-band luminosity $(k+e)$-corrected to $z = 0.0$. The normalization L_0 corresponds to absolute magnitude -22, i.e.

$$\frac{L}{L_0} = 10^{0.4(-22-M_r)}. \quad (19)$$

For reference, typical $(k+e)$-corrections for a completely passive $z = 0.3$ LRG are $(1.51, 1.00, 0.15, -0.05, -0.11)$ in the five bands, and for a $z = 0.55$ LRG these are $(2.73, 1.59, 0.77, 0.05, -0.15)$. If the LRG has some constant low level of star formation, the $(k+e)$-corrections are $(0.86, 0.92, 0.15, -0.04, -0.10)$ from $z = 0.3$ and $(1.04, 1.40, 0.73, 0.05, -0.13)$ from $z = 0.55$. In practice, $(k+e)$-corrections are obtained by considering the observed value of $g-i$ for each galaxy, and doing linear interpolation using its relationship to the predicted observer-frame $g-i$ values for the completely passive and the passive plus star-forming models at that redshift (at $z = 0.3$, the models predict $g-i = 2.30$ and 2.14 for the two models, respectively; at $z = 0.55$, they predict $g-i = 2.79$ and 2.53). The pivot points selected here are $z_\mathrm{pivot} = 0.3$ and $r_\mathrm{pivot} = 20\,h^{-1}$ Mpc.

We have performed a least-squares fit of this $w_{\delta+}(r_\mathrm{p})$ to eight LRG samples: the SDSS LRGs split into six samples (the three bins in luminosity and two in redshift), and the 2SLAQ LRGs split into a faint and bright sample (separated at $M_r = -22.0$). We have converted the observable $w_{\mathrm{g}+}(r_\mathrm{p})$ to $w_{\delta+}(r_\mathrm{p})$ by dividing by the bias of the density tracer. For details on the bias determinations, see Section 6. Note that the bias determination assumed $\sigma_8 = 0.751$; if one wishes to have a constraint on $w_{\delta+}$ for other values of σ_8 it is necessary to multiply the measurement of A_0 in Table 4 by $\sigma_8/0.751$.

The relation $w_{\delta+}(r_\mathrm{p}) = w_{\mathrm{g}+}(r_\mathrm{p})/b_\mathrm{g}$ is the 'obvious' way to do the conversion from correlation functions involving galaxies to those involving matter, but it is worth considering the specific assumptions this makes. It is valid provided that (i) galaxies are locally linearly biased, i.e. the probability distribution for $g(\boldsymbol{r})$ conditioned on a particular realization of the density field depends only on $\delta(\boldsymbol{r})$ and not on δ at other locations, and that the dependence of the mean galaxy density is linear, $\langle g(\boldsymbol{r})\rangle|_\delta = b_\mathrm{g}\delta(\boldsymbol{r})$ and (ii) the intrinsic shear of a galaxy depends only on the surrounding density field (or equivalently on the tidal field, which contains the same information) and not on the placement of the galaxies, $P(\gamma^\mathrm{I}|\delta) = P(\gamma^\mathrm{I}|\delta, g)$ (i.e. specifying the positions of other galaxies provides no additional information not in the density field). Note that the dependence of intrinsic shear on the density field is allowed to be non-local. Given these two assumptions we may write, for $\boldsymbol{r} \neq \boldsymbol{0}$,

$$\begin{aligned}
\xi_{\mathrm{g}+}(\boldsymbol{r}) &= \left\langle \tilde{\gamma}^\mathrm{I}_+(\boldsymbol{0}) g(\boldsymbol{r})\right\rangle = \left\langle [1+\delta(\boldsymbol{0})]\gamma^\mathrm{I}_+(\boldsymbol{0}) g(\boldsymbol{r})\right\rangle \\
&= \int \mathcal{D}\delta\ \mathcal{D}g\ P(\delta, g)\left\langle \gamma^\mathrm{I}_+(\boldsymbol{0})\right\rangle|_{\delta,g}[1+g(\boldsymbol{0})]g(\boldsymbol{r}) \\
&= \int \mathcal{D}\delta\ P(\delta)\left\langle \gamma^\mathrm{I}_+(\boldsymbol{0})\right\rangle|_\delta \langle [1+g(\boldsymbol{0})]g(\boldsymbol{r})\rangle|_\delta \\
&= \int \mathcal{D}\delta\ P(\delta)\langle \gamma^\mathrm{I}_+(\boldsymbol{0})\rangle|_\delta \langle 1+g(\boldsymbol{0})\rangle_\delta \langle g(\boldsymbol{r})\rangle|_\delta \\
&= \int \mathcal{D}\delta\ P(\delta)\left\langle \gamma^\mathrm{I}_+(\boldsymbol{0})[1+g(\boldsymbol{0})]\right\rangle_\delta b_\mathrm{g}\delta(\boldsymbol{r}) \\
&= b_\mathrm{g}\left\langle \gamma^\mathrm{I}_+(\boldsymbol{0})[1+g(\boldsymbol{0})]\delta(\boldsymbol{r})\right\rangle = b_\mathrm{g}\xi_{\delta+}(\boldsymbol{r}). \quad (20)
\end{aligned}$$

Here the first two lines only involve definitions; the third line uses assumption (ii) to remove the conditioning of $\langle\gamma^\mathrm{I}_+(\boldsymbol{0})\rangle$ on g; the fourth line makes use of assumption (i) that the galaxy density depends locally on the matter density to split the expectation value $\langle[1+g(\boldsymbol{0})]g(\boldsymbol{r})\rangle|_\delta$; the fifth line uses the linearity of the biasing from assumption (i) to introduce b_g, and uses assumption (ii) to combine two of the expectation values into $\langle\gamma^\mathrm{I}_+(\boldsymbol{0})[1+g(\boldsymbol{0})]\rangle_\delta$ and the last line again only use definitions. The projected (two-dimensional) relation $w_{\delta+}(r_\mathrm{p}) = w_{\mathrm{g}+}(r_\mathrm{p})/b_\mathrm{g}$ then follows. (Here $\int\mathcal{D}\delta$ represents a functional integral over realizations of the density field.)

Table 4. The best-fitting parameters to equation (18) using SDSS and 2SLAQ LRGs. Error bars are 95 per cent confidence limits. The first set of fit parameters uses the most conservative cut on transverse separation. The $\Delta\chi^2$ value in the second to last columns is the improvement in χ^2 relative to no GI correlation, and the Δd.o.f. value indicates the number of parameters in the fit. The amplitude A_0 is given in units of $0.01\,h^{-1}$ Mpc. The $\Delta\chi^2_i$ values in the last column indicate the degradation of χ^2 used to compute the 95 per cent confidence limits on A_0, α, β and γ, respectively. These are greater than 3.84 for one parameter because of noise in the covariance matrix (see text).

Fit region	$A_0/(0.01\,h^{-1}$ Mpc)	α	β	γ	χ^2/d.o.f.	$\Delta\chi^2/\Delta$d.o.f.	$\Delta\chi^2_i$
			Fits to SDSS+2SLAQ				
$r_\mathrm{p} > 11.9\,h^{-1}$ Mpc	$+6.0^{+2.6}_{-2.2}$	$-0.88^{+0.31}_{-0.34}$	$+1.51^{+0.73}_{-0.69}$	$-1.00^{+2.40}_{-3.19}$	33.3/28	171.8/4	4.38, 4.74, 4.16, 4.47
$r_\mathrm{p} > 7.5\,h^{-1}$ Mpc	$+6.4^{+2.5}_{-2.1}$	$-0.85^{+0.24}_{-0.25}$	$+1.41^{+0.66}_{-0.63}$	$-0.27^{+1.88}_{-2.46}$	42.8/36	215.8/4	5.10, 4.89, 5.07, 5.02
$r_\mathrm{p} > 4.7\,h^{-1}$ Mpc	$+5.9^{+2.3}_{-2.0}$	$-0.73^{+0.19}_{-0.19}$	$+1.48^{+0.64}_{-0.63}$	$-0.56^{+2.02}_{-2.74}$	54.9/44	219.2/4	5.04, 5.08, 4.92, 5.57
			Fits to SDSS only				
$r_\mathrm{p} > 11.9\,h^{-1}$ Mpc	$+7.1^{+3.4}_{-2.7}$	$-0.95^{+0.32}_{-0.35}$	$+1.43^{+0.73}_{-0.71}$	$+1.94^{+4.75}_{-4.52}$	21.3/20	173.9/4	4.49, 4.67, 4.27, 4.27
$r_\mathrm{p} > 7.5\,h^{-1}$ Mpc	$+7.4^{+2.9}_{-2.4}$	$-0.88^{+0.24}_{-0.25}$	$+1.31^{+0.67}_{-0.66}$	$+2.39^{+4.52}_{-4.30}$	27.9/26	208.7/4	4.66, 5.13, 4.91, 4.66
$r_\mathrm{p} > 4.7\,h^{-1}$ Mpc	$+6.6^{+2.7}_{-2.2}$	$-0.74^{+0.19}_{-0.18}$	$+1.44^{+0.63}_{-0.62}$	$+1.81^{+4.52}_{-4.40}$	34.0/32	213.3/4	4.88, 5.10, 4.66, 5.00

Gaussianity is not assumed; however, Gaussianity combined with scale-independent bias (defined by $b_g = \sqrt{\xi_{gg}/\xi_{\delta\delta}}$) and unit stochasticity $r_g = 1$ would imply the validity of assumption (i) since they completely specify the two-point behaviour of the galaxy field. We also note that (i) implies b_g = constant and $r_g = 1$. Of our assumptions, (i) is consistent with (though not uniquely proven by) simulation results suggesting b_g = constant and $r_g = 1$ down to $\sim 5\,h^{-1}$ Mpc (Tasitsiomi et al. 2004); at smaller scales there is a hint of decrease in the bias. The status of assumption (ii) is unknown; however, since galaxy alignments are expected to be determined by tidal fields it is physically reasonable. In the future it would be desirable to do a more detailed analysis, perhaps fitting the $w_{g+}(r_p)$ results directly to simulations; for this reason the correlation functions are given in Appendix A. We have also not attempted to use the conversion $w_{\delta+}(r_p) = w_{g+}(r_p)/b_g$ at smaller scales than the 4.7–7.5 h^{-1} Mpc bin, although these inner bins are provided in the data tables.

We perform several fits to equation (18). In each case, since the galaxies used to trace the ellipticity field do not all have the same luminosity or redshift, we actually fit

$$w_{\delta+}(r_p) = A_0 \frac{\langle r_p^\alpha \rangle}{r_{pivot}^\alpha} \frac{\langle L^\beta \rangle}{L_0^\beta} \frac{\langle (1+z)^\gamma \rangle}{(1+z_{pivot})^\gamma}, \quad (21)$$

where the luminosity and redshift averages are taken over the galaxies in the sample, and the r_p average is weighted by area (analogously to equation 16). In principle one should also weight the redshift average by the comoving number density of the density tracer (full SDSS LRG or 2SLAQ sample) but in practice the comoving number density is nearly constant for the former and the statistical errors are very large for the latter, so we did not implement a correction for this effect.

The fits were done including the correlations between different radial bins for the same subsample, but *not* including the correlations between different subsamples. The correlations between different radial bins of $w_{g+}(r_p)$ for the same subsample are clearly seen in any of the covariance matrices and are expected because galaxies are clustered. They must be included to get meaningful results. However, we do not expect significant correlations between $w_{g+}(r_p)$ in different subsamples, so long as the intrinsic alignments are sufficiently weak. In order to test this, we computed the correlation coefficients $\rho_{iA,jB}$ by the jackknife procedure, where we have used the i, j, ... indices to denote radial bins and A, B, ... to denote LRG subsamples. We consider the six radial bins used for fits here ($4.7 < r_p < 60\,h^{-1}$ Mpc) and the six SDSS LRG subsamples. This provides 315 cross-correlation coefficients with $A \neq B$. In each case we then calculate the Fisher z coefficient, defined by $\rho_{iA,jB} = \tanh z_{iA,jB}$. These 315 coefficients have a sample mean of $+0.019 \pm 0.008$ and a standard deviation of 0.14. For comparison, with 50 jackknife regions of the same size and Gaussian errors, we should have a standard deviation of $\sim 1/\sqrt{50-3} = 0.15$, and the mean value of the $\{z_{iA,jB}\}$ should be zero if the samples truly are independent. In fact we observe the correct standard deviation and a hint of correlation between bins at only the $\sim$2 per cent level. For the two 2SLAQ LRG bins there are 21 z coefficients with a sample mean of $+0.016 \pm 0.046$ and a standard deviation of 0.21. Therefore we have not included correlations between different samples.

The fit results are shown in Table 4. We have included both SDSS-only and SDSS+2SLAQ constraints; it is clear from the fit that the SDSS LRG sample provides essentially all of the constraint on α and β, with the addition of 2SLAQ providing significant new information about the redshift evolution parameter, γ. This is not surprising since the 2SLAQ sample is small but adds a large baseline in redshift. Note that the error bars on A_0 are rather non-Gaussian, so the apparent $\sim 6\sigma$ effect is actually stronger than that (see the $\Delta\chi^2$ values).

The error bars in the table require some explanation. The usual way of constructing error bars on a single parameter is to change its value until the χ^2 (minimized with respect to the other parameters) increases by an amount $\Delta\chi^2 = 3.84$ (the 95th percentile of the χ^2 distribution with one degree of freedom). The problem with this procedure is that if the error bars are determined by resampling (jackknife or bootstrap), the resulting covariance matrix $\mathbf{C}$ of the $w_{g+}(r_p)$ values is noisy (but still unbiased). This leads to a systematic overestimate of $\mathbf{C}^{-1}$ (Hirata & Seljak 2004; Hartlap, Simon & Schneider 2007; Mandelbaum et al. 2006a). In particular, if one has a set of parameters $\{p^i\}$ being fit, the shift $\Delta\chi_i^2$ (i.e. the χ^2 using the true value of parameter i minimized over the other parameters, minus the χ^2 minimized over all parameters, and using the estimated covariance matrix) is not distributed as a χ^2 with one degree of freedom, even for Gaussian-distributed errors. A solution to this problem was proposed by Hirata & Seljak (2004) and Mandelbaum et al. (2006a) who showed that if the data have Gaussian errors, the covariance matrix is obtained from Gaussian data, and the model is linear in the parameters, then the distribution of $\Delta\chi_i^2$ does not depend on the covariance matrix $\mathbf{C}$ and hence can be obtained from a Monte Carlo simulation. Unfortunately their procedure does not apply directly to our problem because we only estimated the covariance matrix entries between $w_{g+}(r_p)$ values for the same subsample – the cross-entries between different subsamples are zero. We have circumvented this problem by doing a Monte Carlo simulation as follows. First, we take the jackknife covariance matrix $\mathbf{C}$ to be the fiducial model and simulate the resampling by the procedure described in appendix D of Hirata & Seljak (2004) with $M = 50$ regions to get a resampled matrix $\hat{\mathbf{C}}$. We then set the cross-entries between different subsamples to zero. We also generate a simulated set of estimated $\{\hat{w}_{g+}(r_p)\}$ according to a Gaussian distribution with mean given by the best-fitting power-law model and covariance $\mathbf{C}$. From this simulated data and simulated covariance matrix, one can then compute a χ^2 surface and find $\Delta\chi_i^2$ for each of the four parameters $\{p^i\}_{i=0}^3$. Repeating this procedure 1024 times allows us to compute the $\Delta\chi_i^2$ distribution for each parameter. The 95th percentile of this distribution is shown in Table 4 for each fitting region and each parameter, and is used to compute the 95 per cent confidence limits on the parameters.

The question naturally arises whether the fits to the LRG signal in Table 4 apply to the GI correlation for the red galaxies fainter than the LRG1 and 2SLAQ-faint samples. Certainly in making a model for the GI correlations for cosmic shear purposes it is necessary to have a model for these fainter objects, which are after all much more numerous. The best way to assess this is to take our LRG models and compare them with the measurements for the L3, L4, L5 and L6 samples of red main galaxies. It is seen from Fig. 2 that our best-fitting value of $\alpha = -0.73$ is consistent with the slope in all four cases, so it remains to test the amplitude. We do this by taking the GI measurements for each of these samples at $r_p > 4.7\,h^{-1}$ Mpc and fitting to them a power law

$$w_{\delta+}(r_p) = w_{\delta+}(r_{pivot}) \left(\frac{r_p}{r_{pivot}} \right)^\alpha, \quad (22)$$

where α is fixed to -0.73 and the normalization $w_{\delta+}(r_{pivot})$ is allowed to vary to minimize the χ^2. The resulting amplitudes are shown in Table 5. The L5 and L6 samples actually include some of the SDSS LRGs, so only the comparisons for L3 and L4 represent an independent test of the power-law model. There are detections at

Table 5. The GI correlation amplitude measured from the L3–L6 red main samples of galaxies, and that predicted by the best LRG fit (to SDSS + 2SLAQ, $r_p > 4.7\,h^{-1}$ Mpc data). The pivot radius is $r_{pivot} = 20\,h^{-1}$ Mpc. Note that the L5 and L6 samples have some overlaps with the LRG sample, so that for these samples the two columns are not independent. Errors shown are 95 per cent confidence limits, which for 50 jackknife regions, six radial bins and one parameter (the amplitude) being fitted correspond to $\Delta\chi^2 = 5.02$.

Sample	$w_{\delta+}(r_{pivot})$ (h^{-1} Mpc)}	
	Measured (95 per cent confidence limit)	Predicted from LRGs
L3.red	$+0.035 \pm 0.032$	$+0.004$
L4.red	$+0.013 \pm 0.019$	$+0.013$
L5.red	$+0.024 \pm 0.022$	$+0.044$
L6.red	$+0.144 \pm 0.078$	$+0.132$

$>2\sigma$ for the L3, L5 and L6 red samples, although the significance is far greater for L6 than for the others. We have also displayed, in the last column, the amplitude predicted by the best LRG fit, after converting the Petrosian magnitudes measured for the SDSS main galaxies to model magnitudes by dividing by 0.8 (the fraction of the flux captured by the Petrosian method for a typical elliptical galaxy; Blanton et al. 2001). This amplitude is consistent with all of the samples at the 95 per cent confidence level.

8 COMPARISON TO THEORY AND SIMULATIONS

In this section we compare our results to analytical and simulation-based models of intrinsic alignments.

8.1 Analytical models

It is worth comparing the results of this analysis to theoretical expectations. Hirata & Seljak (2004) presented an analytic 'linear passive' model for red galaxies, which assumes that a galaxy's ellipticity is a linear function of the local tidal quadrupole when the galaxy forms and then remains unchanged. In this case we expect that on linear scales we should have $P_{\delta,\tilde{\gamma}^I}(k, z) \propto k^{n_s^{\rm eff}} D(z)$, where $n_s^{\rm eff}$ is the scalar spectral index corrected for the transfer function, i.e. $n_s^{\rm eff} = n_s + 2{\rm d}[\ln T(k)]/{\rm d}\ln k$, and $D(z)$ is the growth factor. The redshift dependence is simply the growth factor because δ increases but $\tilde{\gamma}^I$ does not, and the scale dependence is simply that of the underlying power spectrum. [This should be equivalent to equation (18) of Hirata & Seljak (2004), since there $\bar{\rho} \propto (1+z)^3$, $\bar{D}(z) \equiv (1+z)D(z)$, and $P_\delta^{\rm lin}(k, z) \propto k^{n_s^{\rm eff}} D^2(z)$. There is still a factor of $(1+z)^2$ that is missing from equations (14)–(18) of Hirata & Seljak (2004) because of the conversion from comoving to physical scale in the potential–density relation.] Transforming to real space, this predicts

$$\alpha = -2 - n_s^{\rm eff} \quad \text{and} \quad \gamma = \frac{{\rm d}\ln D(z)}{{\rm d}\ln(1+z)}. \tag{23}$$

[There is a 2 instead of a 3 in α because $w_{\delta+}(r_p)$ is a projected quantity and hence is obtained from $P_{\delta,\tilde{\gamma}^I}(k)$ by a two-dimensional Fourier transform.] For a ΛCDM cosmology, this predicts that γ should rise from -1 at high redshift (matter domination) to 0 in the far future (Λ domination). Across the range of redshifts considered here, 0.2–0.7, we expect $\gamma \sim -0.7$. The prediction for α depends somewhat on scale since $n_s^{\rm eff}$ is not constant. We can find the value of α relevant to our observations by taking $P_{\delta,\tilde{\gamma}^I}(k) \propto P_\delta^{\rm linear}(k)$ and using the Hankel transform

$$w_{\delta+}(r_p) = -\frac{1}{2\pi}\int P_{\delta,\tilde{\gamma}^I}(k)\,J_2(kr_p)k\,{\rm d}k \tag{24}$$

to get $w_{\delta+}(r_p)$. Measured across the range from 11.9 to $60\,h^{-1}$ Mpc (i.e. using the largest scale cut-off from Table 4), we find $\alpha = -0.65$ for the fiducial cosmology. Including smaller scales leads to an increase in α because the power-spectrum curves downward, ${\rm d}^2[\ln P(k)]/{\rm d}(\ln k)^2 < 0$: we have $\alpha = -0.52$ over the range (7.5–60)h^{-1} Mpc, and $\alpha = -0.41$ over the range 4.7–60 h^{-1} Mpc. The linear model does not give a prediction for β, which requires an understanding of how the proportionality constant between ellipticity and tidal field relates to the luminosity.

Our results for red galaxies are entirely consistent with the prediction $\gamma = \gamma_{\rm passive} \sim -0.7$, although given the large error bars in Table 4 this is not a particularly impressive accomplishment. From a practical perspective, we have at least set an upper limit on γ, which enables upper bounds on contamination to be placed in cosmic shear investigations. From a theoretical perspective, we are still unable to answer perhaps the most interesting question: is γ larger or smaller than the passive evolution prediction? A value of $\gamma > \gamma_{\rm passive}$ would imply that the intrinsic alignments of red galaxies were greater in the past, and were being reduced, perhaps due to relaxation, merger or figure rotation processes that destroy pre-existing correlations. Conversely, a value of $\gamma < \gamma_{\rm passive}$ would imply that some process was causing the LRGs to align themselves with the large-scale density field, even at low redshift where LRGs are generally believed to be passively evolving.

By contrast, the linear theory predictions for α are only in marginal agreement with observations, with the data giving a smaller (more negative) α. The discrepancy is not significant if one uses the range 11.9–60 h^{-1} Mpc; however, one finds a discrepancy of $\Delta\chi^2 = 9.02$ ($p = 0.005$ using the distribution from the Monte Carlo simulations) if one includes data down to $7.5\,h^{-1}$ Mpc or $\Delta\chi^2 = 13.11$ ($p < 10^{-3}$) down to $4.7\,h^{-1}$ Mpc. The direction of this disagreement is what one would expect if non-linear clustering on small scales enhanced $w_{\delta+}(r_p)$, since this would tilt α to more negative values than predicted by linear theory. Indeed if one substitutes the non-linear power spectrum $P_\delta^{\rm nl}(k)$ of Smith et al. (2003) into equation (24) then the predicted values of α are -0.72, -0.68 and -0.67 for $r_{p,\rm min} = 11.9$, 7.5 and $4.7\,h^{-1}$ Mpc, respectively. These are in very good agreement ($\leqslant 1\sigma$) with the measured slopes; however, the theoretical justification for believing $P_{\delta,\tilde{\gamma}^I}(k)$ to trace the matter power spectrum in the non-linear regime is dubious.

The data on GI correlation for blue galaxies are too noisy to constrain their shape, so we have not attempted to compare this to theoretical models. We also note that the main theory for alignments of these galaxies, namely the tidal torque theory (Peebles 1969; Doroshkevich 1970; White 1984), generically predicts zero GI correlation up to second order in perturbation theory (Hui & Zhang 2002; Hirata & Seljak 2004). Thus more detailed theoretical calculations will be necessary to predict the scale dependence of $w_{\delta+}(r_p)$ for blue galaxies.

8.2 Simulations

The GI contamination to the lensing signal has been investigated in simulations by Heymans et al. (2006b). They used ΛCDM *N*-body simulations populated using the Cooray & Milosavljević (2005) conditional luminosity function and several different models for determining the galaxy (as opposed to halo) ellipticity. They then computed the GI correlations using various models: an 'elliptical'

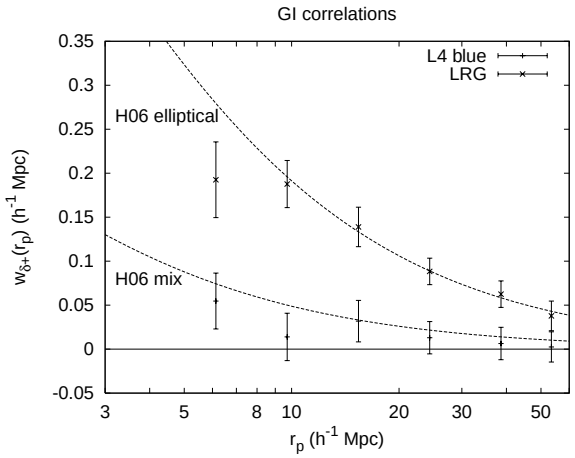

Figure 9. The GI correlation functions $w_{\delta+}(r_p)$ for the full SDSS LRG sample and the L4 blue sample, with the galaxy-to-density conversion using biases of 1.99 and 1.12, respectively. The lines are the curves from Heymans et al. (2006b) at $z = 0.27$, interpreted using the procedure in Appendix B. The median redshift of the LRGs is $z_{\rm med} = 0.27$; the L4 blue galaxies have $z_{\rm eff} = 0.12$, although we expect that evolution between 0.12 and 0.27 would make a small effect.

model for which galaxies were assigned the same ellipticity magnitude and direction as the parent haloes; a 'spiral' model for which they were considered to be disks with some random misalignment with the parent halo angular momentum vector; and a 'mix' model with a mixture of the above. They concluded that only the mix model was consistent with the measurements from Mandelbaum et al. (2006a).

Here it is possible to do a more detailed comparison. In Appendix B, we derive the conversion from the intrinsic shear–lensing shear correlation functions measured by Heymans et al. (2006b) to $w_{\delta+}(r_p)$. We have applied this conversion to the elliptical and mix models, and plotted these in Fig. 9. Overplotted are the $w_{\delta+}(r_p)$ data for the LRGs (median magnitude $\sim$2 magnitudes brighter than $L_\star$) and the L4 blue galaxies (i.e. $\sim L_\star$). The LRG data are consistent with the Heymans et al. (2006b) 'elliptical' model, which is the one with the strongest GI correlation. This may seem surprising since the 'elliptical' model was designed to be a maximal estimate of GI, in the sense that the galaxies were assumed to trace the ellipticity of their host haloes perfectly – one would expect that in the real Universe there would be some misalignment. However, the 'elliptical' model is also averaged over a range of halo masses. Since LRGs typically occupy the most massive haloes, and simulations have suggested that the density–halo ellipticity correlation is stronger at high masses (Hopkins, Bahcall & Bode 2005), it is possible that Heymans et al. (2006b) would have found a much stronger GI correlation if they had only considered LRGs. Simulation results broken into luminosity bins should thus be a priority: until they are available we cannot say whether our LRG measurements confirm the Heymans et al. (2006b) 'elliptical' model, or if there is substantial misalignment in the real Universe that fortuitously results in agreement with Heymans et al. (2006b) because of their lower typical halo mass. In any case we note that LRGs show the strongest alignment signal of all galaxy types considered and make up only a small fraction of any flux-limited sample of galaxies, so for a realistic weak lensing survey the GI contamination would be lower. The more abundant $L_\star$ blue galaxies are consistent (within 2σ) of either zero alignment or the Heymans et al. (2006b) 'mix' model, and it is evident that more data will be needed to distinguish these possibilities.

We are not aware of any simulation results that explore the luminosity dependence of the GI correlation. Studies of *cluster* alignments in *N*-body simulations (Hopkins et al. 2005) find a preferential alignment of the major axis of the cluster with the direction to neighbouring clusters with a strength that increases with halo mass. This is qualitatively consistent with what we observe for the alignments of LRGs, which increase with luminosity, but a quantitative comparison would require one to populate the haloes with galaxies, assign ellipticities, and convert alignment angles to density–shape correlation functions; each of these (but especially the latter two) is a significant source of uncertainty.

9 ESTIMATES OF CONTAMINATION

In principle, with knowledge of the GI correlation scaling with luminosity, colour, redshift and transverse separation, combined with knowledge of the joint luminosity–colour–redshift distribution for a particular survey, we can predict the contribution of GI contamination to the measured cosmic shear power spectrum. In principle, this contamination then carries over to an underestimate of σ_8 or, if the evolution of the amplitude is measured to constrain the equation of state of dark energy, there will be errors in the measurement of w_0 and w_a. In future work, we will attempt to quantify more precisely the effects on the dark energy parameter estimates. For now, we merely present the fractional contamination of the cosmic shear power-spectrum measurement for model surveys with realistic redshift and luminosity distributions, and present a prescription for marginalizing over GI uncertainties in measurements of σ_8.

9.1 Contamination models

To make a prediction of contamination to cosmic shear results, we start with a flux limit, and must assume our model fits for intrinsic alignment amplitude as a function of separation, redshift and luminosity; a luminosity function as a function of spectral type; the underlying cosmology (to get the distance modulus); and $(k + e)$-corrections. From this, we can predict the redshift distribution and the magnitude of the GI correlation contribution to the measured cosmic shear power spectrum. In principle, there is also a correction associated with the types of magnitudes used, e.g. Petrosian versus model. For example, the Petrosian system typically misses $\sim$20 per cent of the flux for well-resolved elliptical galaxies (Blanton et al. 2001). Since the GI signal for red galaxies scales as roughly $L^{1.5}$, this would translate into roughly a 30 per cent error in the GI amplitude, which is small compared to the redshift extrapolation uncertainty in our models. To the extent that it matters, users of these models should note that our contamination estimate for red galaxies is fitted to the LRGs, for which we used model magnitudes; for blue galaxies the constraints on GI are so weak that changes of this order are unimportant.

For the *r*-band luminosity function as a function of spectral type (including luminosity evolution), and for *k*-corrections, we rely on the results from COMBO-17 for $0.2 < z < 1.2$ (Wolf et al. 2003). For a typical cosmic shear survey that is dominated by galaxies with $0.8 < z < 1.2$, the galaxies that are most important for the intrinsic alignments are those at the lower end of the redshift range, where our assumptions about luminosity evolution, etc. are most likely to be valid. For the purposes of this work, the spectral types 1 and 2 in that paper are considered 'red', types 3 and 4 are considered 'blue'. The reason for this distinction is that at $z = 0$, integration of the

Table 6. The four GI models used here to assess contamination. The power-law indices are defined by $w_{\delta+}(r_p) \propto r_p^{\alpha}(1+z)^{\gamma}$. The amplitudes are normalized to $\sigma_8 = 0.751$; for cosmologies with different values of σ_8, the bias of the density tracer scales as $b \propto \sigma_8^{-1}$ and the GI contamination scales as $w_{\delta+} \propto \sigma_8$. 'Fractional contamination' here is defined by C_l^{GI}/C_l^{GG}.

	Model	Galaxy type	Power-law indices α	γ	$w_{\delta+}(20\,h^{-1}\,\mathrm{Mpc}, z=0.3)$ (h^{-1} Mpc)	Fractional contamination $R<23, l=500$	$R<24, l=500$
A	Pessimistic	Red	−0.71	+1.47	$+0.056(L/L_0)^{1.58}$	−0.420	−0.332
		Blue	−0.71	+1.47	+0.028 (L3–L5); +0.61 (L6)		
B	Central	Red	−0.73	−0.56	$+0.059(L/L_0)^{1.48}$	−0.103	−0.065
		Blue	−0.73	−0.70	+0.005 (L3–L5); +0.25 (L6)		
C	Optimistic	Red	−0.73	−0.56	$+0.059(L/L_0)^{1.48}$	−0.042	−0.021
		Blue	−0.73	−0.70	0 (L3–L5); +0.25 (L6)		
D	Very optimistic	Red	−0.73	−3.29	$+0.055(L/L_0)^{1.43}$	−0.034	−0.015
		Blue	−0.73	−3.29	0 (L3–L5); +0.03 (L6)		

templates to obtain observed AB $u-r$ colours (which were used in this paper for colour separation) suggests that all type 1 and nearly all type 2 galaxies would have been classified as red, whereas types 3 and 4 would have been classified as blue. At redshift 0.1–0.25, the classification of the type 2 template as red versus blue is no longer clear, but this uncertainty is in part due to certain features of the spectrum below 300 nm redshifting into the u band. These features have changed significantly in updated versions of the spectra used by the COMBO-17 team, since the templates of Wolf et al. (2003) were found to be inadequate for full galaxy classification,[4] so we define our correspondence between SDSS and COMBO-17 types using the $z=0$ colour (which is not susceptible to influence by these uncertainties in the $\lambda < 300$ nm portion of the spectrum). With this classification scheme, roughly 25 per cent of the galaxies in a flux-limited survey to $R=24$ are classified as red.

The intrinsic alignment signal for the red galaxies is very well constrained at $z \sim 0.3$, with the major uncertainty being the scaling of the signal with redshift. The situation is very different for the blue galaxies for which we have no detection, and for which we only have a low-redshift constraint: the GI correlation for these objects may be near present upper limits, or alternatively could be negligible. In light of these uncertainties, we have defined four different models, all based on the fits at $r_p > 4.7\,h^{-1}$ Mpc.

(1) In the 'pessimistic' model A, we assume that the redshift scaling of GI for the red galaxies is the 95 per cent confidence upper limit from the SDSS + 2SLAQ fit with $r_p > 4.7\,h^{-1}$ Mpc, $\gamma = +1.47$. The GI values for the blue galaxies are taken to have the same radial scaling α and redshift scaling γ as for the red galaxies, with the amplitude taken to be the 95 per cent confidence upper limit from SDSS main. The use of the same radial scaling α is motivated by the expectation that the alignment on large scales should trace the tidal field, which has the same spatial dependence for all types of galaxies. A single amplitude is fitted to the L3–L5 blue galaxies to improve statistics since there is no sign of a detection in any of these bins. A separate amplitude is used for the L6 blue galaxies as these have a marginal detection when α is fixed.

(2) In the 'central' model B, we use the best-fitting values of amplitudes and power-law indices α, β, γ from Table 4 using both SDSS and 2SLAQ and including radii down to $4.7\,h^{-1}$ Mpc. For the blue galaxies we use the same value of α, as explained above, but fix γ to the passive value, $\gamma_{\mathrm{passive}} = -0.7$ and use the best fit rather than worst case value for the amplitude. The L3–L5 galaxies are combined, just as for model B.

(3) In the 'optimistic' model C, we treat the red galaxies and the L6 blue galaxies just as for model B. We assume the L3–L5 blue galaxies have no GI signal, since none is required by the data. (We do not view the detection in the L6 blue galaxies as robust since the significance is $<2.5\sigma$ and only appears in one of the four blue bins.)

(4) In the 'very optimistic' model D, we take the minimum value of γ allowed by SDSS + 2SLAQ at the 2σ level ($\gamma = -2.81$), and use the values of the other parameters that minimize the χ^2 constrained to fixed γ: $A_0 = 0.056, \alpha = -0.73$ and $\beta = 1.44$. Just as for model C, we assume no alignment for L3–L5 blue galaxies. We take the 2σ lower limit for L6 blue galaxies.

Note that in each model, we used constrained (i.e. α and γ fixed) fits to the blue galaxies in each of the luminosity bins in the $r_p = (4.7\text{–}60)\,h^{-1}$ Mpc regime. The best-fitting amplitudes $A = w_{\delta+}(20\,h^{-1}\,\mathrm{Mpc})$ assuming the model A scale dependence ($\alpha = -0.71$) are $+0.003 \pm 0.026$, $+0.017 \pm 0.022$, -0.015 ± 0.035 and $+0.27 \pm 0.25\,h^{-1}$ Mpc for the L3, L4, L5 and L6 blue samples, respectively, where 95 per cent confidence errors are given. For model B/C/D scale dependence ($\alpha = -0.73$), we find very similar results: $w_{\delta+}(20\,h^{-1}\,\mathrm{Mpc}) = +0.003 \pm 0.026$, $+0.017 \pm 0.022$, -0.015 ± 0.034 and $+0.27 \pm 0.25\,h^{-1}$ Mpc for the same samples. For presentation (Table 6) we have rescaled all values to $z=0.3$ using the specified choice of γ and the mean redshifts of the samples (see Table 3). In each case we have used the 'L3–L5 blue' amplitude for the blue galaxies fainter than L3, since we have no better constraint for them (the SDSS main sample does not probe an interesting volume at fainter luminosities).

The models are summarized in Table 6, along with estimates of the fractional GI contamination as quantified by the ratio C_l^{GI}/C_l^{GG}. For most cosmic shear studies, model A can be taken as a '2σ' estimate of the GI contamination. Model B should be viewed as a 'best guess', with the caveat that we have no detection of GI in the L3–L5 blue samples. If the reason for this non-detection is that the GI signal in these samples is *much* less than the current upper limits, then model C may be more realistic than B.

As an example of these models, we show in Fig. 10 the GI contamination for a cosmic shear survey that measures galaxies down to $R=24$ (median redshift 0.6). The results in the figure are not necessarily representative of cosmic shear surveys to the specified depth, since the sources will not all be weighted equally (and some may be rejected from the analysis due to being poorly resolved, or having poorly constrained photo-zs with the particular bandpasses used in the survey). The fractional contamination C_l^{GI}/C_l^{GG} is −33,

[4] Christian Wolf, private communication.

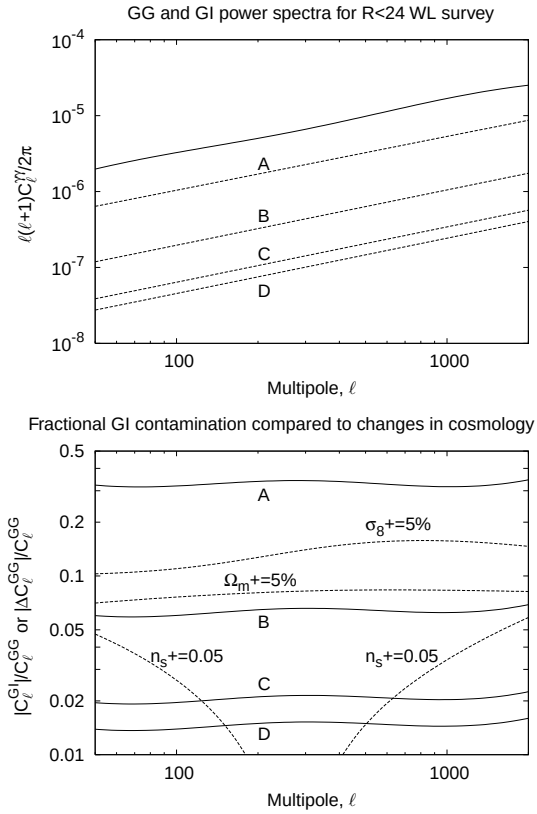

Figure 10. Upper panel: The cosmic shear power spectrum (solid line) and GI power spectra (dashed lines) for all galaxies with $R < 24$. We plot the absolute value of GI since it is negative for all models. Lower panel: The fractional contamination of the power spectrum $|C_l^{\rm GI}|/C_l^{\rm GG}$ (solid lines), compared to the change produced by several changes in the cosmological parameters $|\Delta C_l^{\rm GG}|/C_l^{\rm GG}$ (dashed lines). This ranges from ∼33 per cent for model A to ∼1.5 per cent for model D. We have plotted the range out to $l = 2000$ ($k \sim 1\,h\,{\rm Mpc}^{-1}$ at the typical source redshift) since at smaller scales we cannot convert from $w_{g+}(r_p)$ to $w_{\delta+}(r_p)$ (see Section 7). For the variations of cosmological parameters, Ω_m is varied at fixed $\Omega_m h^2$ and n_s is varied at fixed σ_8.

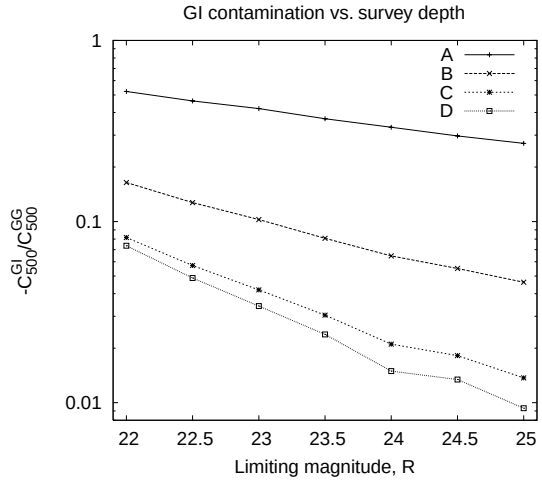

Figure 11. The GI contamination at $l = 500$ for the four models as a function of survey depth. We considered all galaxies with R-band magnitude less than the specified cut-off, and $z < 1.2$.

−6.5, −2.1 and −1.5 per cent for models A–D, respectively, at $l = 500$ (these values are given in Table 6). As can be seen from the figure, these fractions are almost independent of l because the intrinsic alignment power spectrum $P_{\delta,\tilde{\gamma}^I}(k) \propto k^{-2-\alpha} = k^{-1.27\pm0.19}$ (95 per cent confidence limit) has roughly the same k dependence as the matter power spectrum. This was actually measured for the LRGs; setting the blue galaxies (which have no detection) to the same slope as the red galaxies was a modelling assumption. The fraction of the contamination coming from blue galaxies is 93, 69, 3.3 and 0.4 per cent for models A–D. It is clear that refining the models for blue galaxies should be a high priority for future work since these dominate the uncertainty in the GI estimates (though it is not clear whether they dominate the GI contamination). Note that the contamination estimates presented are on the power spectrum; the fractional contamination on the amplitude σ_8 will be less by a factor of ∼2 since the power spectrum is roughly proportional to σ_8^2. In particular for the survey to $R = 24$ at $l = 500$, the reduction in shear power spectrum $C_l^{\gamma\gamma}$ is equivalent to changing σ_8 by $\Delta\sigma_8 = -0.10$, -0.02, -0.005 and -0.004 for models A–D, respectively.

Integrated over all scales, the GI contamination we predict in the pessimistic model A results in a 1σ error for a survey measuring all galaxies to $R = 24$ with combined shape and measurement noise $\gamma_{\rm rms} = 0.3$ over a region of sky of only $4\,{\rm deg}^2$. Thus if model A is correct then GI contamination may already be important for the current generation of lensing surveys. Models B, C and D predict an error of 1σ for sky coverage of 100, 1000 and 2000 deg^2, respectively; thus even in the optimistic cases GI contamination will be significant and will have to be removed in future surveys.

We have also investigated the dependence of the contamination estimates on the magnitude cut, as shown in Fig. 11. For this calculation the COMBO-17 luminosity function was also used, hence a cut-off in the redshift distribution at $z = 1.2$ was imposed. The amount of contamination generally decreases with survey depth: for our 'central' model it is twice as severe at $R_{\rm max} = 22.5$ than at $R_{\rm max} = 24$.

We also could have constructed a more extreme pessimistic model than model A by taking the 95 per cent confidence upper limit in each of bins L3, L4 and L5 separately; for the above-mentioned toy cosmic shear survey to $R = 24$, this 'AA' model leads to −41 per cent contamination at $l = 500$ instead of −33 per cent. Such a model would of course be unrealistically pessimistic for surveys covering a broad range in galaxy luminosity, since by taking the 2σ upper limit in each luminosity bin and averaging these numbers we obtain a $>2\sigma$ upper limit on the average.

9.2 Constraining σ_8

Finally we come to the issue of greatest practical importance in the near term: how should one account for GI contamination in σ_8 measurements from cosmic shear? We have already seen that if our more pessimistic models are correct then the contamination may be significant compared to the uncertainties in some of the recent measurements. In this case it is essential to correct for the GI effect and include the range of allowed GI models in determining the error bars on σ_8. Since the present surveys are measuring a single amplitude σ_8 (with some dependence on other cosmological parameters such as Ω_m) what we really need is a probability distribution for $\Delta\sigma_8$ (which also may depend on other parameters) over which one can marginalize. In future surveys that measure several parameters we will need a multivariate distribution. Therefore we view the model here as a first step: it leaves much room for future work to reduce

the uncertainties in $\Delta\sigma_8$, particularly to pin down the several σ tails of the distribution (which are treated rather crudely here), and to extend the model to incorporate multiple parameters.

In constructing this distribution for $\Delta\sigma_8$, we first note that the error bar on the GI contamination is highly asymmetric due to the nature of the redshift extrapolation: if the redshift exponent γ is very negative or zero there is very little contamination, but if it is positive then it is possible to have very large contamination. In all cases the central model predicts relatively small contamination (a few per cent) but the pessimistic model based on the 2σ upper limit to γ could be a factor of several worse, and the optimistic models are a factor of several better. Therefore we recommend that for measurements of σ_8 one should marginalize over contamination $\Delta\sigma_8$ with a lognormal probability distribution. To be more explicit, we recommend the following prescription: for the distribution of galaxy luminosities, redshifts and colours in a particular cosmic shear survey, compute the pessimistic (A) and central (B) power spectra $C_l^{\rm GI}$ (A, B). Then compute the induced error $\Delta\sigma_8$(A, B) for these two models. One can then write

$$\sigma_8(\text{observed}) = \sigma_8(\text{true}) - x, \tag{25}$$

where x is lognormally distributed:

$$P(x) = \frac{1}{\sqrt{2\pi}\,\sigma\,x} \exp\left[-\frac{1}{2\sigma^2}\left(\ln\frac{x}{x_0}\right)^2\right] \tag{26}$$

for $x > 0$ and $P(x) = 0$ for $x < 0$. The median of this distribution is the central model, i.e. $x_0 = -\Delta\sigma_8$(B), and the standard deviation is chosen to place the pessimistic model at 2σ:

$$\sigma = \frac{1}{2}\ln\frac{\Delta\sigma_8(\text{A})}{\Delta\sigma_8(\text{B})}. \tag{27}$$

Usually one uses a Markov Chain Monte Carlo (MCMC) method to estimate cosmological parameters from a combination of data sets; in this case one should marginalize over x with the prior given by equation (26). This could be done by including x as a nuisance parameter in the MCMC, or (probably faster) by including the integral over x as part of the cosmic shear likelihood function.

Note that this method has not explicitly used the optimistic models in constructing the probability distribution for x, assuming instead that the distribution in $\ln x$ is symmetric. In practice this is probably not a serious deficiency for two reasons. First, for the cases we have investigated, the ratio of contamination for model A to model B is indeed similar to that of model B to model D (5.1 versus 4.3 for $R < 24, l = 500$; 4.1 versus 3.0 for $R < 23, l = 500$), i.e. the error in 'log contamination' is close to symmetric. Secondly, the error in σ_8 in the optimistic and very optimistic models is usually <0.01, which is negligible compared to the purely statistical errors from the current generation of weak lensing surveys. This means that while the details of the pessimistic tail of the distribution matter (because they affect whether cosmic shear can rule out high σ_8), the details of the optimistic tail do not – the optimistic tail might as well be 'piled up' at zero contamination.

We believe the method described here is adequate for the current generation of cosmic shear surveys in which the cosmological constraint is a single amplitude, generally reported as a value of σ_8 with some dependence on $\Omega_{\rm m}$. However, it will not be adequate for future surveys that will measure the redshift and scale dependence of the signal, in which the GI contamination must be described by more than one number. Also these surveys will push the statistical errors on the cosmic shear signal to the <1 per cent level, i.e. according to the models presented here the GI contamination will dominate over statistical uncertainty. In order to make use of this data, we will need more external information to better constrain the GI models, or use internal information from the cosmic shear surveys themselves to simultaneously constrain the pure lensing signal, the GI signal and (if applicable) the II signal. Strategies for this are discussed in the literature (Hirata & Seljak 2004; King 2005; Bridle & King 2007).

In summary, we have constructed a basic model for the GI contamination that can be practically integrated into current and near-future lensing constraints on σ_8. It is a minimal model, making the simplest assumptions in some cases (e.g. power-law scale, luminosity and redshift dependence). Nevertheless, it fulfils the basic criteria of being consistent with the data and covering the range of allowed values of the most important uncertain parameter (γ). Aside from improving the statistical uncertainties on GI model parameters, future work covering a range of redshifts would also improve the robustness of the model by enabling us to constrain more model parameters, such as deviations from the power law $\sim(1+z)^\gamma$ or different values of α and γ for blue and red galaxies.

10 CONCLUSIONS

In this work, we have attempted to further characterize the correlation between the intrinsic shear and the density field on both small and large scales. To this end, we have characterized the strength of this alignment as a function of galaxy transverse separation, luminosity (focusing on the bright end, where it is most prominent), colour and redshift to $z \sim 0.6$. In addition, we have established that the GI amplitude of LRGs is not significantly different for BG and non-BG galaxies for scales above the virial radius, though we were unable to verify the degree to which this statement is true for cases of large luminosity gap. We found that the shape–density alignment signal for red galaxies increases strongly as a function of the luminosity. The scale dependence $w_{\rm g+}(r_{\rm p}) \propto r^{-0.73\pm0.17}$ is very similar to that of the matter power spectrum, which is expected if galaxy alignment is determined by the local tidal field. Our findings that the density–shape alignment effect is present for non-BGs up to large scales imply that our original hypothesis that the effect is due only to BGs needs to be revised.

There is no detection of GI correlation for blue galaxies, with the possible exception of the very brightest bin (L6 blue). In this case there is a $\sim 2.4\sigma$ detection if one fixes the scaling with $r_{\rm p}$ to the value for the red galaxies. If one does a 'blind' search over power laws $r_{\rm p}^\alpha$ (as done in Section 5.1) the signal is not statistically significant. When combined with the fact that we have no detection in the lower luminosity blue bins which have many more galaxies, we believe that the L6 blue GI signal is not robust, and observationally many of these galaxies are quite close to the blue versus red division. In any case the L6 blue galaxies are very rare (despite their luminosity, they comprise <1 per cent of the flux-limited SDSS main sample!) and their measured GI signal would contaminate the toy cosmic shear survey considered in Section 9 at the <0.1 per cent level if taken at face value. Much more important for the cosmic shear programme are the numerous fainter ($L \sim L_\star$) blue galaxies. The GI signal for these objects is consistent with zero; however, if the signal is near our upper limits, they may affect the observed shear power spectrum by of the order of 10 per cent for surveys to $R = 24$. Reducing the uncertainties in the measurements for the $L \sim L_\star$ blue galaxies should be a priority for future work. It would also be desirable to learn more about the GI correlation $w_{\delta+}(r_{\rm p})$ at very small scales where linear galaxy biasing (which underlies the methodology of Section 7) breaks down; this would likely involve both the $w_{\rm g+}(r_{\rm p})$ measurements presented in Appendix A and

simulation or halo model results on the relation between galaxies and mass at small scales.

We have presented several models of the GI signal in Section 9, spanning the range from pessimistic assumptions (model A) to optimistic (model D). We believe these models will be useful for others in comparing against other data sets and/or estimating levels of contamination in various surveys. In particular it would be useful for lensing surveys to repeat the calculations in Section 9, taking into account their actual redshift/luminosity/colour distribution instead of the toy distributions used here.

These results should also be useful in comparing against simulations to determine the physical cause behind this effect, especially in conjunction with previous results on II contamination and future work on contamination of three-point functions, which may give additional power to discriminate between intrinsic alignment models. A fuller understanding of the physics behind these effects may allow us to extend these fitting relations to higher redshift than is currently allowed by the data.

Methods have been proposed (e.g. King 2005) to remove intrinsic alignment contamination using parametrized GI and II correlation models. Our determination of the redshift evolution and luminosity scaling of GI correlations will help make these methods more feasible in practice.

Finally, the GI models presented here (and any improved models that incorporate future observations) may be used to determine criteria for excluding galaxies from future cosmic shear surveys to obtain a galaxy sample with the lowest possible level of intrinsic alignment contamination. Surveys with imaging data in multiple bands should fairly easily be able to remove the bright red galaxies that seem to show the strongest GI contamination. Future work with simulations will be necessary to determine the efficacy of this plan. This plan is most likely to be effective if the blue galaxy contamination is found in future work to be negligibly small; if this is not the case, then more sophisticated methods to remove GI such as templates (King 2005) and separation based on redshift dependence (Hirata & Seljak 2004) will be essential to realizing the promise of the cosmic shear programmes.

ACKNOWLEDGMENTS

CMH is a John Bahcall Fellow in Astrophysics at the Institute for Advanced Study. RM is supported by NASA through Hubble Fellowship grant #HST-HF-01199.02-A awarded by the Space Telescope Science Institute, which is operated by the Association of Universities for Research in Astronomy, Inc., for NASA, under contract NAS 5-26555. MI acknowledges partial support from the Hoblitzelle Foundation and a Clark Award at the University of Texas, Dallas. US is supported by the Packard Foundation, NASA NAG5-1993 and NSF CAREER-0132953.

We thank Christian Wolf for clarification regarding the templates used by the COMBO-17 survey in Wolf et al. (2003). We would also like to thank the anonymous referee for helpful comments.

Funding for the creation and distribution of the SDSS Archive has been provided by the Alfred P. Sloan Foundation, the Participating Institutions, the National Aeronautics and Space Administration, the National Science Foundation, the US Department of Energy, the Japanese Monbukagakusho and the Max Planck Society. The SDSS web site is http://www.sdss.org/.

The SDSS is managed by the Astrophysical Research Consortium (ARC) for the Participating Institutions. The Participating Institutions are The University of Chicago, Fermilab, the Institute for Advanced Study, the Japan Participation Group, The Johns Hopkins University, the Korean Scientist Group, Los Alamos National Laboratory, the Max-Planck-Institute for Astronomy (MPIA), the Max-Planck-Institute for Astrophysics (MPA), New Mexico State University, University of Pittsburgh, University of Portsmouth, Princeton University, the United States Naval Observatory and the University of Washington.

REFERENCES

Abazajian K. et al., 2003, AJ, 126, 2081
Abazajian K. et al., 2004, AJ, 128, 502
Abazajian K. et al., 2005, AJ, 129, 1755
Adelman-McCarthy J. et al., 2006a, ApJS, 162, 38
Adelman-McCarthy J. et al. 2006b, ApJS, submitted
Agustsson I., Brainerd T. G., 2006, ApJ, 644, L25
Azzaro M., Patiri S. G., Prada F., Zentner A. R., 2007, MNRAS, 376, L43
Bacon D. J., Refregier A. R., Ellis R. S., 2000, MNRAS, 318, 625
Bernstein G. M., Jain B., 2004, ApJ, 600, 17
Bernstein G. M., Jarvis M., 2002, AJ, 123, 583
Bernstein G. M., Norberg P., 2002, AJ, 124, 733
Blanton M. R. et al., 2001, AJ, 121, 2358
Blanton M. R., Lin H., Lupton R. H., Maley F. M., Young N., Zehavi I., Loveday J., 2003a, AJ, 125, 2276
Blanton M. R. et al., 2003b, AJ, 125, 2348
Blanton M. R. et al., 2005, AJ, 129, 2562
Bridle S., King L., 2007, preprint (arXiv:0705.0166)
Brown M. L., Taylor A. N., Hambly N. C., Dye S., 2002, MNRAS, 333, 501
Brown M. L., Taylor A. N., Bacon D. J., Gray M. E., Dye S., Meisenheimer K., Wolf C., 2003, MNRAS, 341, 100
Bruzual G., Charlot S., 2003, MNRAS, 344, 1000
Cannon R. et al., 2006, MNRAS, 372, 425
Catelan P., Kamionkowski M., Blandford R. D., 2001, MNRAS, 320, L7
Cole S. et al., 2005, MNRAS, 362, 505
Cooray A., Hu W., 2002, ApJ, 574, 19
Cooray A., Milosavljević M., 2005, ApJ, 627, L89
Cooray A., Kamionkowski M., Caldwell R., 2005, Phys. Rev. D, 71, 123527
Crittenden R. G., Natarajan P., Pen U.-L., Theuns T., 2001, ApJ, 559, 552
Croft R. A. C., Metzler C. A., 2000, ApJ, 545, 561
Donoso E., O'Mill A., Lambas D. G., 2006, MNRAS, 369, 479
Doroshkevich A. G., 1970, Astrophysics, 6, 320
Eisenstein D. J., Hu W., 1998, ApJ, 496, 605
Eisenstein D. J. et al., 2001, AJ, 122, 2267
Eisenstein D. J. et al., 2005, ApJ, 633, 560
Erben T., Van Waerbeke L., Bertin E., Mellier Y., Schneider P., 2001, A&A, 366, 717
Finkbeiner D. et al., 2004, AJ, 128, 2577
Fukugita M., Ichikawa T., Gunn J. E., Doi M., Shimasaku K., Schneider D. P., 1996, AJ, 111, 1748
Gradshteyn I. S., Ryzhik I. M., Table of Integrals, Series and Products, 5th edn. Academic Press, New York
Gunn J. E., Carr M., Rockosi C., Sekiguchi M. et al., 1998, AJ, 116, 3040
Gunn J. E. et al., 2006, AJ, 131, 2332
Hartlap J., Simon P., Schneider P., 2007, A&A, 464, 399
Heavens A., Refregier A., Heymans C., 2000, MNRAS, 319, 649
Heymans C., Heavens A., 2003, MNRAS, 339, 711
Heymans C., Brown M., Heavens A., Meisenheimer K., Taylor A., Wolf C., 2004, MNRAS, 347, 895
Heymans C. et al., 2005, MNRAS, 361, 160
Heymans C. et al., 2006a, MNRAS, 368, 1323
Heymans C., White M., Heavens A., Vale C., Van Waerbeke L., 2006b, MNRAS, 371, 750
Hirata C. M., Seljak U., 2003a, MNRAS, 343, 459
Hirata C. M., Seljak U., 2003b, Phys. Rev. D, 68, 083002
Hirata C. M., Seljak U., 2004, Phys. Rev. D, 70, 063526
Hirata C. M. et al., 2004, MNRAS, 353, 529
Hoekstra H. et al., 2006, ApJ, 647, 116

Hogg D. W., Finkbeiner D. P., Schlegel D. J., Gunn J. E., 2001, AJ, 122, 2129
Hopkins P. F., Bahcall N. A., Bode P., 2005, ApJ, 618, 1
Hu W., 2002, Phys. Rev. D, 65, 023003
Hui L., Gaztañaga E., 1999, ApJ, 519, 622
Hui L., Zhang J., 2002, preprint (astro-ph/0205512)
Huterer D., 2002, Phys. Rev. D, 65, 063001
Huterer D., Takada M., Bernstein G., Jain B., 2006, MNRAS, 366, 101
Ishak M., 2005, MNRAS, 363, 469
Ishak M., Hirata C. M., 2005, Phys. Rev. D, 71, 023002
Ishak M., Hirata C., McDonald P., Seljak U., 2004, Phys. Rev. D, 69, 083514
Ishak M., Upadhye A., Spergel D., 2006, Phys. Rev. D, 74, 043513
Ivezić Ž. et al., 2004, Astron. Nachr., 325, 583
Jarvis M., Bernstein G. M., Fischer P., Smith D., Jain B., Tyson J. A., Wittman D., 2003, AJ, 125, 1014
Jarvis M., Jain B., Bernstein G., Dolney D., 2006, ApJ, 644, 71
Jing Y. P., 2002, MNRAS, 335, L89
Jing Y. P., Zhang P., Lin W. P., Gao L., Springel V., 2006, ApJ, 640, L119
Kaiser N., 2000, ApJ, 537, 555
Kaiser N., Squires G., Broadhurst T., 1995, ApJ, 449, 460
Kaiser N., Wilson G., Luppino G. A., 2000, preprint (astro-ph/0003338)
King L., 2005, A&A, 441, 47
King L., Schneider P., 2002, A&A, 396, 411
King L., Schneider P., 2003, A&A, 398, 23
Knox L., Song Y.-S., Tyson J. A., 2006, Phys. Rev. D, 74, 023512
Kulkarni G. et al. 2006, MNRAS, submitted
Landy S., Szalay A., 1993, ApJ, 412, 64
Lee J., Pen U., 2001, ApJ, 555, 106
Lee J., Pen U., 2002, ApJ, 567, L111
Lupton R., Gunn J. E., Ivezić Ž., Knapp G. R., Kent S., Yasuda N., 2001, in Harnden F. R. Jr, Primini F. A., Payne H. E., eds, ASP Conf. Ser. Vol. 238, Astronomical Data Analysis Software and Systems X. Astron. Soc. Pac., San Francisco, p. 269
Mandelbaum R. et al., 2005, MNRAS, 361, 1287
Mandelbaum R., Hirata C. M., Ishak M., Seljak U., Brinkmann J., 2006a, MNRAS, 367, 611
Mandelbaum R., Seljak U., Kauffmann G., Hirata C. M., Brinkmann J., 2006b, MNRAS, 368, 715
Mandelbaum R., Hirata C. M., Broderick T., Seljak U., Brinkmann J., 2006c, MNRAS, 370, 1008
Massey R., Refregier A., Bacon D. J., Ellis R., Brown M. L., 2005, MNRAS, 359, 1277
Massey R. et al., 2007, MNRAS, 376, 13
Miralda-Escudé J., 1991, ApJ, 380, 1
Navarro J., Abadi M., Steinmetz M., 2004, ApJ, 613, L41
Padmanabhan N. et al., 2007, MNRAS, 378, 852
Peacock J. A., Dodds S. J., 1996, MNRAS, 280, L19
Peebles P. J. E., 1969, ApJ, 155, 393
Pen U., Lee J., Seljak U., 2000, ApJ, 543, L107
Pier J. R., Munn J. A., Hindsley R. B., Hennessy G. S., Kent S. M., Lupton R. H., Ivezić Ž., 2003, AJ, 125, 1559
Rawlings S. et al., 2004, New Astron. Rev., 48, 1013
Refregier A., 2003, ARA&A, 41, 645
Richards G. et al., 2002, AJ, 123, 2945
Ross N. et al. 2006, MNRAS, submitted
Schlegel D. J., Finkbeiner D. P., Davis M., 1998, ApJ, 500, 525
Schneider P., van Waerbeke L., Mellier Y., 2002, A&A, 389, 729
Seljak U. et al., 2005, Phys. Rev. D, 71, 043511
Sembolini E. et al., 2006, A&A, 452, 51
Smith J. A. et al., 2002, AJ, 123, 2121
Smith R. E. et al., 2003, MNRAS, 341, 1311
Song Y. S., Knox L., 2005, Phys. Rev. D, 71, 024026
Spergel D. N. et al., 2007, ApJS, 170, 377
Stoughton C., Lupton R. H. et al., 2002, AJ, 123, 485
Strauss M. A., Weinberg D. H., Lupton R. H., Narayanan V. K. et al., 2002, AJ, 124, 1810
Takada M., White M., 2004, ApJ, 601, L1
Tasitsiomi A., Kravtsov A. V., Wechsler R. H., Primack J. R., 2004, ApJ, 614, 533
Tegmark M. et al., 2004, ApJ, 606, 702
Tinker J., Norberg P., Weinberg D. H., Warren M. S., 2007, ApJ, 659, 877
Tucker D. et al., 2006, Astron. Nachr., 327, 821
Vale C., Hoekstra H., Van Waerbeke L., White M., 2004, ApJ, 613, L1
Van Waerbeke L. et al., 2000, A&A, 358, 30
Van Waerbeke L., Mellier Y., Hoekstra H., 2005, A&A, 429, 75
Wake D. et al., 2006, MNRAS, 372, 537
White M., 2004, Astropart. Phys., 22, 211
White S. D. M., 1984, ApJ, 286, 38
Wittman D. M., Tyson J. A., Kirkman D., Dell'Antonio I., Bernstein G., 2000, Nat, 405, 143
Wolf C., Meisenheimer K., Rix H. W., Borch A., Dye S., Kleinheinrich M., 2003, A&A, 401, 73
Yang X., van den Bosch F. C., Mo H. J., Mao S., Kang X., Weinmann S. M., Guo Y., Jing Y. P., 2006, MNRAS, 369, 1293
York D. G. et al., 2000, AJ, 120, 1579
Zehavi I. et al., 2005, ApJ, 621, 22
Zhan H., Knox L., 2004, ApJ, 616, L75

APPENDIX A: GALAXY DENSITY–SHAPE CORRELATION FUNCTION DATA

This appendix lists the correlation functions $w_{g+}(r_p)$ for the samples used in our fits, and their correlation coefficients. The table headers describe the subsamples used to trace the intrinsic shear field; the galaxy density ('*g*') was traced using the full sample (i.e. SDSS main, SDSS LRG low-*z*, SDSS LRG high-*z* or 2SLAQ). It is the bias of the latter (described in Section 6) that should be used to convert to $w_{\delta+}(r_p)$. Table A1 lists the measured correlation functions and their error bars, while Table A2 shows the correlation coefficients $\rho[w_{\delta+}(r_p), w_{\delta+}(r'_p)]$ between different radial bins for the same sample. The innermost bin from the 2SLAQ-bright sample did not have enough data to determine a bootstrap error; so this and its correlation matrix elements are marked with a '*' in these tables.

APPENDIX B: RELATION OF LENSING SHEAR–INTRINSIC SHEAR AND DENSITY–INTRINSIC SHEAR CORRELATION FUNCTIONS

The purpose of this appendix is to relate the lensing shear–intrinsic shear correlation function $\langle\gamma^G(z_s)\cdot\gamma^I(z_1)\rangle_\theta$ measured in simulations by Heymans et al. (2006b) to the density–intrinsic shear correlation function $w_{\delta+}(r_p)$ considered in this paper. In particular we would like to know whether the results of Heymans et al. (2006b) are consistent with our observations. In this appendix, we will use z_s for the source-plane redshift and z_1 for the lens-plane redshift (i.e. the redshift at which GI contamination is being assessed) for consistency with Heymans et al. (2006b); however, for consistency with our paper we will write γ^I where Heymans et al. (2006b) would write *e* [defined by their equation (4); note that the ellipticity components before correction for the shear responsivity, which we denote e_i, are denoted by ϵ_i in Heymans et al. (2006b)].

Our conversion proceeds in two steps: first from $\langle\gamma^G(z_s)\cdot\gamma^I(z_1)\rangle_\theta$ to $\langle\kappa(z_s)\gamma^I_+(z_1)\rangle_\theta$, and then from $\langle\kappa(z_s)\gamma^I_+(z_1)\rangle_\theta$ to $w_{\delta+}(r_p)$. The first step is a straightforward but tedious calculus exercise, since γ^G and κ are different derivatives of the lensing potential and hence are simply related in Fourier space; the second step is trivial and involves the usual convergence to surface density conversion from galaxy–galaxy lensing studies.

Table A1. The correlation functions $w_{g+}(r_p)$ for each sample. The first column shows the range of r_p, and the remaining columns show $w_{g+}(r_p)$ and its 1σ uncertainty (i.e. square root of diagonal covariance matrix element). Units are h^{-1} Mpc for all columns.

$r_{p,\rm min} - r_{p,\rm max}$	Main.L3.blue	Main.L4.blue	Main.L5.blue	Main.L6.blue	Main.L3.red	Main.L4.red
0.3–0.6	0.145 ± 0.198	-0.177 ± 0.194	0.494 ± 0.443	-1.127 ± 6.011	0.117 ± 0.330	0.032 ± 0.212
0.6–1.2	-0.081 ± 0.129	0.118 ± 0.108	-0.106 ± 0.215	1.604 ± 1.854	0.259 ± 0.147	0.070 ± 0.100
1.2–2.4	-0.038 ± 0.069	-0.020 ± 0.067	0.100 ± 0.134	1.588 ± 0.761	0.003 ± 0.101	-0.005 ± 0.053
2.4–4.7	0.033 ± 0.035	-0.012 ± 0.035	0.018 ± 0.088	0.590 ± 0.653	0.053 ± 0.057	0.008 ± 0.053
4.7–7.5	0.017 ± 0.034	0.061 ± 0.036	-0.030 ± 0.060	0.948 ± 0.395	0.103 ± 0.048	0.024 ± 0.036
7.5–11.9	0.059 ± 0.042	0.016 ± 0.030	-0.040 ± 0.050	0.585 ± 0.329	0.110 ± 0.042	0.036 ± 0.026
11.9–18.9	-0.000 ± 0.032	0.036 ± 0.026	-0.048 ± 0.046	0.227 ± 0.313	0.073 ± 0.041	0.014 ± 0.024
18.9–29.9	-0.010 ± 0.025	0.015 ± 0.021	-0.000 ± 0.045	0.177 ± 0.214	0.059 ± 0.040	0.011 ± 0.018
29.9–47.4	0.003 ± 0.020	0.007 ± 0.021	-0.007 ± 0.029	0.176 ± 0.155	0.010 ± 0.034	0.008 ± 0.013
47.4–59.6	0.017 ± 0.026	0.003 ± 0.019	0.007 ± 0.034	-0.046 ± 0.164	-0.044 ± 0.035	0.010 ± 0.019
$r_{p,\rm min}$–$r_{p,\rm max}$	Main.L5.red	Main.L6.red	LRG1,low-z	LRG2,low-z	LRG3,low-z	LRG1,high-z
0.3–0.6	0.744 ± 0.224	7.676 ± 1.387	5.075 ± 9.556	1.365 ± 8.740	2.975 ± 6.866	-1.277 ± 8.148
0.6–1.2	0.278 ± 0.127	2.906 ± 0.644	3.590 ± 1.753	1.007 ± 2.188	1.714 ± 3.181	2.784 ± 1.583
1.2–2.4	0.212 ± 0.087	0.956 ± 0.288	1.978 ± 0.873	-0.216 ± 0.606	1.633 ± 0.769	0.370 ± 0.526
2.4–4.7	0.149 ± 0.051	0.619 ± 0.158	1.033 ± 0.327	0.105 ± 0.312	0.957 ± 0.302	0.693 ± 0.242
4.7–7.5	0.039 ± 0.036	0.420 ± 0.132	0.270 ± 0.189	0.182 ± 0.187	0.362 ± 0.190	0.441 ± 0.191
7.5–11.9	0.062 ± 0.028	0.243 ± 0.107	0.274 ± 0.130	0.078 ± 0.164	0.708 ± 0.135	0.388 ± 0.133
11.9–18.9	0.046 ± 0.030	0.306 ± 0.076	0.339 ± 0.100	-0.001 ± 0.100	0.250 ± 0.087	0.349 ± 0.076
18.9–29.9	0.092 ± 0.027	0.239 ± 0.063	0.135 ± 0.063	0.035 ± 0.059	0.209 ± 0.062	0.209 ± 0.071
29.9–47.4	0.036 ± 0.018	0.120 ± 0.060	0.053 ± 0.050	0.106 ± 0.055	0.164 ± 0.043	0.138 ± 0.035
47.4–59.6	0.010 ± 0.016	0.016 ± 0.038	-0.036 ± 0.057	0.115 ± 0.045	0.092 ± 0.041	0.107 ± 0.047
$r_{p,\rm min} - r_{p,\rm max}$	LRG2,high-z	LRG3,high-z	2SLAQ-faint	2SLAQ-bright		
0.3–0.6	-7.429 ± 7.872	21.379 ± 9.708	-3.713 ± 8.009	*		
0.6–1.2	4.603 ± 3.609	7.346 ± 3.589	-3.235 ± 3.722	5.380 ± 3.223		
1.2–2.4	2.940 ± 1.125	2.634 ± 0.792	0.425 ± 1.327	2.717 ± 1.287		
2.4–4.7	1.950 ± 0.444	1.150 ± 0.406	-0.155 ± 0.499	0.598 ± 0.621		
4.7–7.5	0.629 ± 0.296	0.890 ± 0.308	0.506 ± 0.385	-0.230 ± 0.396		
7.5–11.9	0.518 ± 0.208	0.539 ± 0.155	-0.335 ± 0.333	0.469 ± 0.214		
11.9–18.9	0.592 ± 0.113	0.365 ± 0.107	-0.168 ± 0.161	0.087 ± 0.155		
18.9–29.9	0.344 ± 0.103	0.290 ± 0.084	0.004 ± 0.172	-0.020 ± 0.138		
29.9–47.4	0.094 ± 0.080	0.257 ± 0.054	-0.085 ± 0.157	0.209 ± 0.116		
47.4–59.6	0.103 ± 0.077	0.144 ± 0.060	-0.129 ± 0.207	0.112 ± 0.143		

For our first step, we recall that the shear components (+, ×) can be easily converted to E and B modes in Fourier space by

$$\gamma_+^G(\boldsymbol{l}) \pm \mathrm{i}\gamma_\times^G(\boldsymbol{l}) = \mathrm{e}^{2\mathrm{i}\phi(\boldsymbol{l})}\left[\gamma_{\rm E}^G(\boldsymbol{l}) + \mathrm{i}\gamma_B^G(\boldsymbol{l})\right], \tag{B1}$$

where $\phi(\boldsymbol{l}) = \arctan(l_y/l_x)$ is the position angle of $\boldsymbol{l}$, and a similar formula is written for the intrinsic shear. The convergence–density correlation function is then the Fourier transform of the cross-power spectrum,

$$\begin{aligned}\langle\kappa(\boldsymbol{\theta})\gamma_+^{\rm I}(\boldsymbol{0})\rangle &= \int \frac{\mathrm{d}^2\boldsymbol{l}}{(2\pi)^2} C_l^{\kappa\gamma^{\rm I}} \mathrm{e}^{\mathrm{i}\boldsymbol{l}\cdot\boldsymbol{\theta}} \mathrm{e}^{2\mathrm{i}\phi(\boldsymbol{l})} \\ &= -\int_0^\infty \frac{l\,\mathrm{d}l}{2\pi} C_l^{\kappa\gamma^{\rm I}} J_2(l\theta).\end{aligned} \tag{B2}$$

Here we have assumed parity invariance, i.e. that the convergence is correlated only with the E mode of the intrinsic shear. (The latter may have a B mode but this cannot be correlated with a scalar.) We have also chosen $\boldsymbol{\theta}$ to lie along the x-axis (i.e. the axis along which stretching corresponds to positive +-component shear) and used the integral representation of the Bessel function (equation 8.411 of Gradshteyn & Ryzhik 1994). A similar result holds for the $\gamma^G\gamma^{\rm I}$ correlation:

$$\langle\boldsymbol{\gamma}^G(\boldsymbol{\theta})\cdot\boldsymbol{\gamma}^{\rm I}(\boldsymbol{0})\rangle = \int_0^\infty \frac{l\,\mathrm{d}l}{2\pi} C_l^{\kappa\gamma^{\rm I}} J_0(l\theta); \tag{B3}$$

once again we have used only the E mode since the lensing shear γ^G is derived from the scalar density field and has only E modes (aside from small corrections due to non-weak shear or multiple deflections). We have replaced $C_l^{\gamma^G\gamma^{\rm I}} \to C_l^{\kappa\gamma^{\rm I}}$ since $\gamma_{\rm E}^G$ and κ have equal numerical values mode by mode (they are both second derivatives of the lensing potential), and we have a J_0 function instead of $-J_2$ because there is no factor of $\mathrm{e}^{2\mathrm{i}\phi(l)}$ in this equation [the dot product of the lensing and intrinsic shears is unaffected by the angle $\phi(\boldsymbol{l})$ rotation of equation (B1)].

The conversion between equations (B2) and (B3) proceeds as follows. The cross-power spectrum $C_l^{\kappa\gamma^{\rm I}}$ can be obtained from equation (B3) by the Hankel transform pair,

$$C_l^{\kappa\gamma^{\rm I}} = 2\pi \int_0^\infty \langle\boldsymbol{\gamma}^G(\boldsymbol{\vartheta})\cdot\boldsymbol{\gamma}^{\rm I}(\boldsymbol{0})\rangle J_0(l\vartheta)\vartheta\,\mathrm{d}\vartheta, \tag{B4}$$

from which we find

$$\langle\kappa(\boldsymbol{\theta})\gamma_+^{\rm I}(\boldsymbol{0})\rangle = -\int_0^\infty \langle\boldsymbol{\gamma}^G(\boldsymbol{\vartheta})\cdot\boldsymbol{\gamma}^{\rm I}(\boldsymbol{0})\rangle \mathcal{G}(\theta,\vartheta)\vartheta\,\mathrm{d}\vartheta, \tag{B5}$$

where the Green's function is

$$\mathcal{G}(\theta,\vartheta) \equiv \int_0^\infty \mathrm{d}l\, l J_0(l\vartheta) J_2(l\theta). \tag{B6}$$

This Green's function has a closed-form analytical expression that can be obtained using the recursion, differentiation and

Table A2. Correlation matrices for the data shown in Table A1. The unit is per cent (i.e. all correlation matrix elements have been multiplied by 100) for all the data presented in the table. In each of the four blocks of this table, there is an upper (above-diagonal) triangle, which applies to the sample designated 'upper', and a lower (below-diagonal) triangle, which applies to the sample designated 'lower'. Note that the diagonal correlation coefficients are equal to unity (100 per cent).

Main.L3.blue (upper); Main.L4.blue (lower)

100	4	9	−10	22	41	11	47	−1	−15
7	100	2	−15	−6	16	15	1	−12	−19
6	21	100	24	−7	−13	0	−2	−33	−12
−24	12	27	100	10	3	7	8	−7	−16
−18	20	22	33	100	50	24	17	3	5
−13	−10	14	−5	17	100	56	25	1	−8
2	−3	20	3	16	26	100	26	−3	−22
12	−18	12	−16	7	11	37	100	25	−30
1	14	8	−7	16	8	0	20	100	51
−11	10	−13	20	16	−12	7	1	49	100

Main.L5.blue (upper); Main.L6.blue (lower)

100	18	18	6	26	7	−9	−10	−11	−12
26	100	20	−2	10	11	1	5	1	4
−14	11	100	30	25	8	8	−2	−10	16
27	37	9	100	45	40	7	6	5	0
40	42	15	41	100	38	−14	−22	−10	6
33	23	−16	30	46	100	35	8	−7	−2
37	15	8	12	43	37	100	65	19	2
35	16	5	8	15	7	56	100	29	4
43	13	4	0	25	9	18	29	100	47
6	14	−7	5	21	−2	4	24	39	100

Main.L3.red (upper); Main.L4.red (lower)

100	34	−23	−3	6	−22	2	−1	19	9
20	100	16	8	24	−1	−1	−5	3	−9
12	8	100	8	2	26	−5	−5	−4	−7
13	−19	44	100	15	7	18	5	−8	−6
−22	−29	11	55	100	27	7	6	−6	−18
−7	0	8	16	46	100	50	28	4	1
−6	12	1	8	4	19	100	69	8	−7
0	22	−8	1	−2	5	63	100	24	4
25	24	−3	−2	−15	−6	27	46	100	40
17	−4	23	−1	−11	−13	0	−19	18	100

Main.L5.red (upper); Main.L6.red (lower)

100	39	0	14	13	7	−15	−18	−11	8
45	100	15	22	14	13	1	9	−7	−24
34	47	100	37	−18	10	−5	−2	18	−17
40	14	37	100	−21	−14	−14	−20	2	−12
33	31	13	24	100	36	0	16	−2	1
12	−16	11	13	39	100	43	22	15	−25
14	11	8	0	29	53	100	53	32	5
12	11	17	−9	7	17	54	100	44	0
−5	−2	0	−17	−5	8	33	51	100	20
11	0	17	−5	10	7	20	20	32	100

LRG1,low-*z* (upper); LRG2,low-*z* (lower)

100	−8	−23	−8	11	3	−9	−5	−8	9
−13	100	−6	−6	−19	−12	8	9	2	7
−2	16	100	−9	−14	−8	22	9	2	−3
−16	24	4	100	1	23	27	12	13	19
−8	−2	23	11	100	27	13	−6	1	−9
27	−3	−8	−21	4	100	11	−6	3	−2
27	−14	−12	−10	−12	23	100	9	−13	1
29	−5	9	11	6	18	26	100	35	12
−9	0	5	8	7	−12	−3	−10	100	33
8	2	15	12	0	2	12	11	9	100

LRG3,low-*z* (upper); LRG1,high-*z* (lower)

100	−32	5	25	−17	4	3	−4	−24	−4
4	100	14	−5	4	−11	17	2	−15	−25
7	4	100	20	−33	−11	−10	3	−21	0
8	3	−13	100	9	−33	−8	2	−15	−20
1	2	−8	11	100	13	1	2	20	4
−1	11	26	−6	21	100	−11	−2	26	3
7	30	1	16	−15	−11	100	3	−20	−11
−17	8	9	20	0	19	30	100	−11	−20
−27	11	3	26	−5	2	−5	0	100	39
5	10	−2	2	−15	4	1	9	42	100

LRG2,high-*z* (upper); LRG3,high-*z* (lower)

100	10	−3	−10	−5	15	−1	−20	−11	6
18	100	−20	−16	−22	0	−15	−4	2	5
10	2	100	22	5	−6	10	28	16	13
−6	−26	−1	100	−3	14	23	9	−5	−11
−18	9	−16	9	100	18	28	−1	22	11
−11	2	14	3	20	100	41	−9	−1	−8
−9	−19	5	11	7	28	100	0	1	11
3	5	0	10	27	12	1	100	53	44
3	17	23	14	4	11	15	4	100	33
2	29	6	31	21	−17	−6	16	16	100

2SLAQ-faint (upper); 2SLAQ-bright (lower)

100	−39	−9	−3	13	−30	−16	6	−9	0
*	100	−7	7	−11	28	8	−13	5	−15
*	13	100	27	18	−1	−11	13	25	27
*	0	−11	100	19	2	27	6	42	18
*	4	16	30	100	25	20	35	37	32
*	5	6	−18	9	100	27	19	7	−8
*	3	13	31	5	−2	100	44	26	9
*	0	−23	13	−8	−17	24	100	54	37
*	−17	3	13	1	−30	20	58	100	59
*	1	−32	0	18	31	−3	−5	−1	100

orthonormality relations for Bessel functions:

$$\begin{aligned}\mathcal{G}(\theta,\vartheta) &= \int_0^\infty \mathrm{d}l\, l J_0(l\vartheta)\left[-J_0(l\theta)+\frac{2}{l\theta}J_1(l\theta)\right]\\ &= -\int_0^\infty \mathrm{d}l\, l J_0(l\vartheta)J_0(l\theta)+\frac{2}{\theta}\int_0^\infty \mathrm{d}l\; J_0(l\vartheta)J_1(l\theta)\\ &= -\frac{\delta(\theta-\vartheta)}{\theta}+\frac{2}{\theta}\int_0^\infty \mathrm{d}l\int_\vartheta^\infty \mathrm{d}w\; l J_1(lw)J_1(l\theta)\\ &= -\frac{\delta(\theta-\vartheta)}{\theta}+\frac{2}{\theta}\int_\vartheta^\infty \mathrm{d}w\frac{\delta(w-\theta)}{\theta}\\ &= -\frac{\delta(\theta-\vartheta)}{\theta}+\frac{2}{\theta^2}\Theta(\theta-\vartheta),\end{aligned} \tag{B7}$$

where Θ is the Heaviside step function. (The third line has used the fact that $-J_1$ is the derivative of J_0.) Therefore

$$\begin{aligned}\langle\kappa(\boldsymbol{\theta})\gamma_+^{\mathrm{I}}(\mathbf{0})\rangle &= -\langle\boldsymbol{\gamma}^G(\theta)\cdot\boldsymbol{\gamma}^{\mathrm{I}}(\mathbf{0})\rangle\\ &\quad+\frac{2}{\theta^2}\int_0^\theta\langle\boldsymbol{\gamma}^G(\boldsymbol{\vartheta})\cdot\boldsymbol{\gamma}^{\mathrm{I}}(\mathbf{0})\rangle\vartheta\;\mathrm{d}\vartheta.\end{aligned} \tag{B8}$$

Heymans et al. (2006b) fit their results to the functional form

$$\langle\boldsymbol{\gamma}^G(z_{\mathrm{s}})\cdot\boldsymbol{\gamma}^{\mathrm{I}}(z_1)\rangle_\theta = \frac{A\mathcal{E}}{\theta+\theta_0}, \tag{B9}$$

where A and θ_0 are free parameters and $\mathcal{E}=D_l D_{\mathrm{ls}}/D_{\mathrm{s}}$ is the lensing strength. Plugging this into equation (B8) yields

$$\langle\kappa(z_s)\gamma_+^I(z_1)\rangle_\theta = A\mathcal{E}\left(\frac{1}{\theta+\theta_0} - \frac{2}{\theta} + \frac{2\theta_0}{\theta^2}\ln\frac{\theta+\theta_0}{\theta_0}\right). \quad \text{(B10)}$$

Our second step is to convert this into a density–intrinsic shear correlation function. To do this, we recall the Born (single-deflection) approximation for the convergence,

$$\kappa(z_s) = \frac{3\Omega_m H_0^2}{2c^2}\int dr\, \mathcal{E}\delta(r), \quad \text{(B11)}$$

where δ is the density perturbation. If the correlations between $\kappa(z_s)$ and the intrinsic shear field at a particular redshift z_l arise near z_l, then we may change variables from distance from the observer r to radial separation $\Pi = r - r(z_l)$, multiply both sides by the intrinsic shear field, and take the average:

$$\langle\kappa(z_s)\gamma_+^I(z_1)\rangle_\theta = \frac{3\Omega_m H_0^2}{2c^2}\mathcal{E}\int d\Pi\, \xi_{\delta+}(r_p, \Pi), \quad \text{(B12)}$$

where $r_p = r\theta$ is the separation and we can pull $\mathcal{E}$ (which varies slowly with lens redshift) out of the integral because only a small range at $z \approx z_l$ contributes. The last integral is $w_{\delta+}(r_p)$, so combining with equation (B10) we have

$$w_{\delta+}(r_p) = \frac{2c^2 A}{3\Omega_m H_0^2}\left(\frac{1}{\theta+\theta_0} - \frac{2}{\theta} + \frac{2\theta_0}{\theta^2}\ln\frac{\theta+\theta_0}{\theta_0}\right). \quad \text{(B13)}$$

This is the equation we have used to compare the Heymans et al. (2006b) results to ours in Section 8.2.

This paper has been typeset from a TEX/LATEX file prepared by the author.